Chapter-5

Production and processing of cellulose phosphate from viscose for 3D printing application

Motivation

In this chapter, phosphorylated cellulose (PC) gel was produced from viscose cloths (VC) to process it through additive manufacturing. VC is a readily accessible and cost-effective source of cellulose which can be directly utilised for phosphorylation without prior treatment. 3D printing is a commercially scalable technique that can produce complex structures and rapidly prototype for the emerging application of cellulose phosphate. Furthermore, the chemical modification of PC gels for in-situ synthesis of MoS_2 on the 3D-printed system for remediation of dyes and pathogenic bacteria from wastewater were studied.

Challenges

- *Traditional routes, such as TEMPO-oxidation, carboxymethylation, and ammonium persulfate modification for the production of functionalised cellulose, are expensive, energy-intensive, time-consuming and produce more carbon footprints.*
- *Most of the studies reported for cellulose phosphorylation utilizes highly concentrated and harmful acids, leading to the degradation of cellulose.*

Solutions addressed in this chapter

- *A scalable, simple and cost-effective route for the production of PC gel developed using agro-chemicals.*
- *The phosphorylation method is a more environmentally friendly alternative for cellulose gel production than the traditional TEMPO oxidation process.*
- *PC gels with high water stability and heat crosslinking ability are produced, excluding the application of external costly and toxic crosslinking chemicals. The heat crosslinking ability mechanism was investigated using solid-state NMR and XPS.*
- *PC gels also have shear-thinning properties with a power law index of less than 1, representing its suitability for 3D printing applications.*
- *In-situ growth of MoS_2 into PC gels provides dual functionality, promoting photodegradation of methylene blue (MB) and inactivation of bacteria*

The work in this chapter is published as:

1. *R. Ranjan, R. Rai, K. Naik, A. S. Parmar, and P. Dhar, "Scalable phosphorylated cellulose production with improved environmental sustainability, crosslinkability and processability using 3D bioprinting for dye remediation,"* ***Int. J. Biol. Macromol****., p. 130577, Mar. 2024, doi: 10.1016/j.ijbiomac.2024.130577.*
2. *R. Ranjan, R. Rai, K. Naik, A. S. Parmar, and "In-situ Growth of MoS_2 on 3D Printed Phosphorylated Cellulose for Simultaneous Dye Degradation and Microbial Inactivation"* ***(Communicated****).*

Graphical Abstract

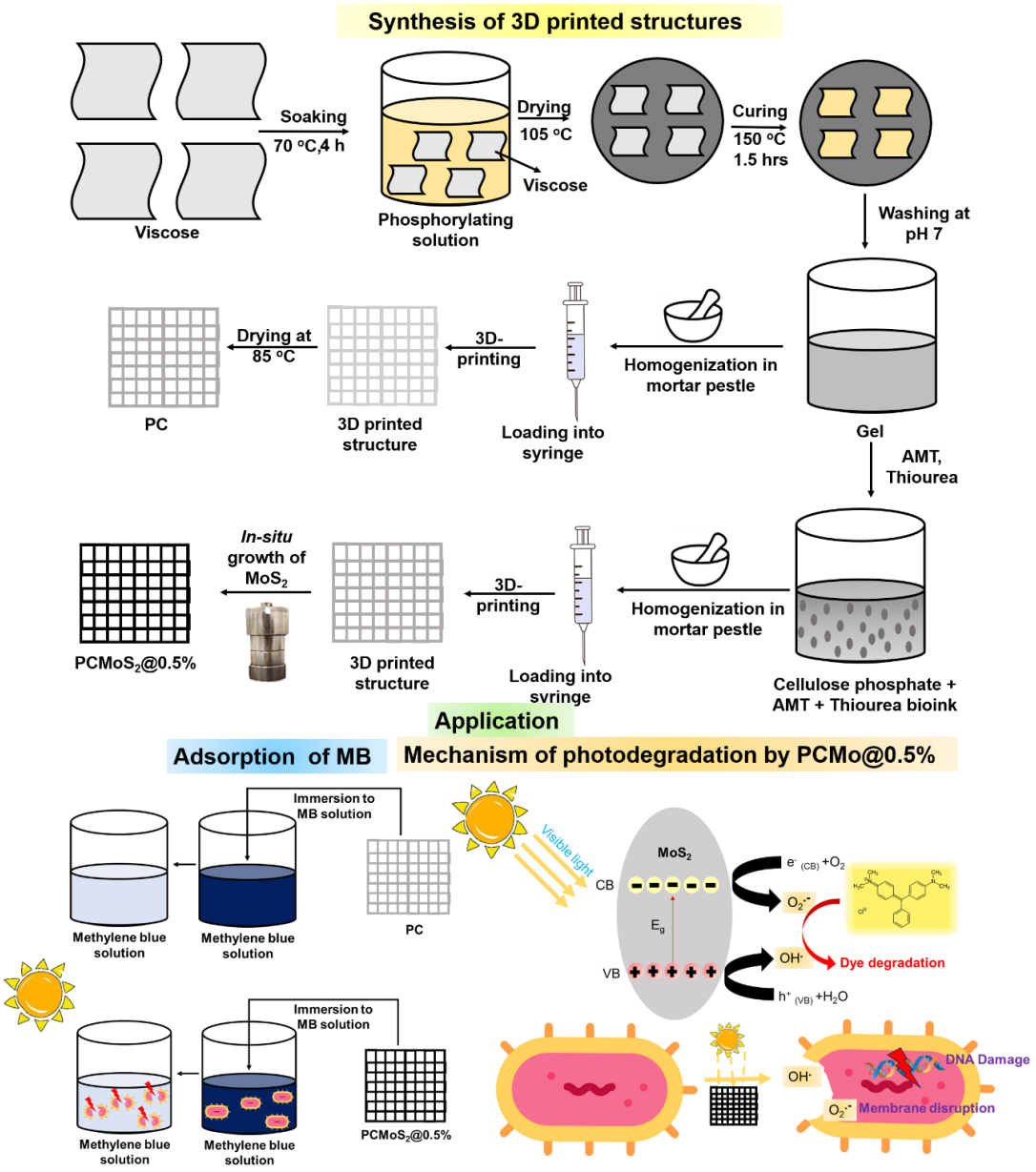

5.1 Introduction

Cellulose is the most abundantly available natural polymer derived from renewable resources such as agricultural biomass, plants, bacteria, algae and animals, with interesting physiochemical and structural properties [84]. It can be processed into various micro and nano morphological forms such as cellulose nanofiber (CNF), cellulose nanocrystals (CNC), micro-fibrillated cellulose (MFC), nano-fibrillated cellulose (NFC), and BC [461]. Out of these, MFC has become popular in recent years with high market demand and potential application in various emerging sectors because of its strong reinforcement capability, tuneable morphology, crystallinity, and improved thermal and barrier properties. Due to its abundant hydroxyl groups, functionalization of MFC has been extensively carried out *via* oxidation, acetylation, sulphonation, nitration, alkylation, along with *in-situ* and *ex-situ* modification using nanoparticles [462]. Oxidation of MFC using 2,2,6,6-tetramethylpiperidine-1-oxyl (TEMPO) combined with sonication, micro-fluidization, grinding, high-pressure homogenisation, or ball milling are widely used traditional methods for oxidation [463]. LCA of the above-mentioned chemical modification processes shows high cumulative energy demand (37.4 MJ) and global warming potential (1.9 kg CO_2 eq.), with requirement of harsh chemicals which makes it expensive, and difficult to scale-up for commercial application [67,464,465]. Therefore, an alternative sustainable and scalable route for producing chemically functionalized MFC with reduced energy demands and lowered environmental impacts is need of the hour. Among all MFC functionalization strategies, phosphorylation has gained immense popularity recently due to the introduction of flame retardancy, high CC, swelling properties and gel-forming ability in developed cellulose composites [466].

Utilization of several phosphorylating agents such as phosphorous acid, PA, phosphorous oxychloride, phosphorous pentoxide, ammonium dihydrogen phosphate, di-ammonium hydrogen phosphate (DAHP), and sodium dihydrogen phosphate have been reported in literature [255]. Ghanadpour et al. [242] reported phosphorylation followed by high-pressure homogenisation of softwood pulp (1 wt. %) for the production of highly charged (1540 μmol/kg) and thermally stable paper. Recently, Rol et al. [154] produced phosphorylated CNF with high solid content (10 wt. %) using DAHP processed in a twin extruder to develop flame retardant nano-papers. Kokol et al. synthesised phosphorylated NFC and NCC using PA, resulting in improved CC of 1173 mmol/kg and 1038 mmol/kg, respectively [205]. Hence, utilization of acids have known to cause the degradation of cellulose backbone resulting in poor mechanical strength. Therefore, an alternative and environmentally benign route for phosphorylation of cellulose is necessary. Boukind et al. produced phosphorylated paper with high charge density (7000 mmol/kg) using Giant Reed for MB dye adsorption with a capacity of ~1200 mg/g [277]. The production of phosphorylated gels with high negative charge makes them a promising candidate for adsorption of cationic dyes and heavy metals ions such as Cd^{+2}, Pb^{+2}, U^{+6}, and Cr^{+3}, potential bio-adsorbent for wastewater remediation [466].

Various adsorbents, catalysts, biochar, metallic organic frameworks, covalent organic frameworks, and filtration methods have been developed using cellulose or modified cellulose for the purpose of dye remediation. In recent years, 3D printing has gained popularity due to its ability to create complex structures quickly, with high precision and cost-effectiveness. With the increased research and development in printable biomaterials, bio-composites, bio-nanomaterials, and smart materials, 3D

printing is now widely used in various fields, including biomedicine, biomedical, tissue engineering, food technology, healthcare, and wastewater treatment [467,468]. For examples, Yuan et al. developed cellulose-alginate-based 3D printed structures with maximum MB adsorption capacity of 66.3 mg/g and could be efficiently reused for 8 cycles [14]. In another study, Shojaeiarani et al. developed CNC, alginate, and poly(ethylene) oxide-based 3D structures to remove MB and malachite green (MG) with maximum removal efficiency of 95.2 % and 82.3 % respectively [15]. Abdelhamid et al. also fabricated 3D printed composites using bio-ink derived from $Zn(NO_3)_2 \cdot 6H_2O$ and cellulose to remove MB and Rhodamine with removal efficiency of 96 % [16]. Zhang et al. developed aerogel from cellulose and iron nanoparticles *via* 3D printing to remediate MB at efficiency of 88.5 % [17]. All these studies utilised cellulose based composites infused with biopolymers or nanoparticles with crosslinking agent processed through a scalable 3D printed system for potential dye remediation. Chemical crosslinking agents are expensive and pose toxicity risks. Therefore, PC could serve as a viable alternative, as it can be physically crosslinked through heat treatment. The utilization of PC with tuneable CC for potential dye removal overcomes the requirement of any other additives and in combination with 3D printing provides a scalable rapid prototyping technology for wastewater treatment. Moreover, till date studies utilizing high CC PC gels processed through 3D printing techniques and their subsequent utilisation for dye remediation, have not been reported yet. VC, a regenerated cellulose is selected as a substrate for phosphorylation because of its low cost, easy availability, well-defined industrial-scale production, lacks lignin or hemicellulose content eliminating the need for additional processing steps and its suitability for gel production [20]. Unlike the processing of lignocellulosic biomass,

which requires extraction and separation of cellulose, in this study PC gels was directly produced through a single-step phosphorylation followed by 3D printing. In contrast to previous research using costly phosphorylating chemicals with limited recovery rates, our method utilises economical alternatives, rendering it a more cost-effective and scalable technology. Few studies are reported on the development of phosphorylated viscose by Kumari et al. [18] [19] using plasma routes for developing antimicrobial fabrics using zinc pyrithione. Furthermore, the developed PC was further utilized for *in-situ* modification with molybdenum disulfide (MoS_2) *via* hydrothermal treatment. *In-situ* modification with MoS_2 is responsible for simultaneous photodegradation as well as antibacterial properties, which enhances its effectiveness in eliminating organic dyes and pathogenic microbes such as *E. coli* and *S. aureus*. MoS_2 is a type of two-dimensional transition-metal dichalcogenide. It has three atomic layer structures with strong Mo-S covalent bonds within the layers and weak Van der Waals force (S-Mo-S bonds) between individual layers. Due to the presence of active catalytic sites, large surface area, photocatalytic, semiconductor, electronic, and optical properties, MoS_2 have gathered huge attention in the last decade [469,470]. MoS_2 displays different phases depending on the conditions, such as the semiconducting *2H* and metallic *1T* phases. The different phases of MoS_2 have unique electronic properties that play a crucial role in determining its functionality across various applications. MoS_2 has been known for its capacity to produce reactive oxygen species (ROS) when exposed to light or certain chemical environments. This property has garnered interest in areas such as photocatalysis and biological applications. The production of ROS, such as singlet oxygen, superoxide radicals, and hydroxyl radicals, can cause oxidative stress in biological systems or promote oxidation reactions in catalytic processes [471]. Shen et

al. developed a composite of BC and MoS_2 for the remediation of malachite green and catechol violet dyes as well as inactivation of *S. aureus* and *E. coli* bacteria (99.9 %) from wastewater [374]. Tang et al. in their recent study, developed MoS_2 in three phases (*1T*/*2H*-MoS_2 (180 °C), *1T*-MoS_2 (140 °C), and *2H*-MoS_2 (220 °C). Among all, the *1T*-MoS_2 phase resulted in maximum adsorption of MB of 98.7% [472]. Similarly, Neto et al., in their study, developed a BC-MoS_2 composite for the photodegradation of MB and Cr^{+4} with 96 % and 88 % removal efficiency [14]. Yu et al. synthesised cellulose-palladium nanoparticle-based composites for MB degradation, which shows 99 % catalytic activity and five times reusability [473].

The antibacterial properties of MoS_2 may be due to the inherent photocatalytic characteristics of MoS_2. When MoS_2 is exposed to light sources, it leads to the production of ROS. These reactive oxygen species play a crucial role in destroying or deactivating microorganisms by causing lysis of their cell membranes. When the membrane breaks, it causes the removal of phospholipids and compromises the structural stability of the lipid membrane in bacteria [429]. Zhang et al. synthesised MoS_2 using ultrasonic, hydrothermal, and intercalation methods to study the antibacterial activity against *E. coli*. Intercalation exhibited the highest sterilisation rate, reaching 99 % within 180 minutes. However, hydrothermal and ultrasonic synthesized MoS_2 resulted in a 62% and 33% sterilization rate [474]. Ci et al. developed PLC nanofiber composites containing MoS_2/ZnS, demonstrating removal rates of 96.03 % for *S. aureus* and 99.09 % for *E. coli* [475]. Real wastewater contains dyes, metals, salts, and pathogens in high volume and requires a scalable technology for remediation with high throughoutput. Therefore, a combination of 3D printed structures with MoS_2

can be utilized for both photodegradation and bacterial inactivation for both batch and continuous operational modes.

In this study we present a facile production and 3D printing-based scalable processing of PC using agro-chemicals with high consistency, CC and low energy requirements. The environmental impacts of developed PC gel production were evaluated through LCA analysis and compared with traditional TEMPO-oxidised gel. The rheological studies show improved viscoelastic and shear thinning behaviour of PC gels making it suitable for processing through 3D-printing. Interestingly, phosphate groups in PC were found to cross-link upon heat treatment, which was mechanistically investigated through solid-state NMR, XPS and FTIR spectroscopy studies. Furthermore, the developed PC gel was mixed with ammonium molybdate trihydrate (AMT) and thiourea for *in-situ* growth of MoS_2 *via* hydrothermal technique. It was done to improve the adsorption capacity of PC as well as to introduce properties like photodegradation and antibacterial properties. PCMo@0.5 % structures were further used to investigate the photodegradation and bacterial inactivation under continuous mode using plug flow reactor. The catalyst's reusability was also assessed and proven to be highly effective in the photodegradation of MB for five cycles, achieving a degradation efficiency of 92 %. The developed PCMo@0.5 % composites also showed strong antibacterial responses against Gram positive, *E. coli* and Gram negative, *S. aureus*. The 3D-printed PC structures stand out for their easy recovery from dye solutions due to structural integrity, simplifying the material regeneration process, high recyclability and thereby reduce the cost for dye remediation. The consistent degradation of MB under light exposure and its ability to simultaneously inhibit bacterial growth indicates its potential application in real wastewater treatment. In

Chapter 5, the subdivision comprises two sections. The first section (Section 5.2) explains about production of PC gel, evaluation of their 3D printability through rheological studies, followed by evaluation of physiochemical, structural and morphological properties, and potential dye adsorption is studied. The second section (Section 5.3) is dedicated to study related to 3D-printed structures of *in-situ* modified MoS_2-PC gels followed by material characterization, and their application in adsorption, and photodegradation of MB and inactivation of pathogenic bacteria such as *E. coli* and *S. aureus* in both batch and continuous mode.

5.2 Results and discussion

5.2.1 PC gel production and evaluation of physicochemical properties

Figure 5.1*(a-e)**, summarizes the overall scheme for PC fabrication, mechanism of phosphorylation followed by its 3D-printing and thermal induced-crosslinking. The hydroxyl groups present in cellulose are phosphorylated using low-cost agro-chemicals which results in production of transparent PC gel with interesting physio-chemical properties. The phosphorylation is carried out following solid-state curing process in which molten urea plays crucial role in swelling, impregnation of phosphorylating agents and preventing degradation of cellulose. It was observed that time and temperature for curing severely affects the surface charge as well as colour of fabricated gels. The gel exhibited good transparency, viscosity, consistency and suitability for 3D printing. Upon heat treatment, the gel demonstrated covalent crosslinking between P-O-P groups (Figure 5.1*(e)**) which resulted in improved thermal stability. PC gels produced after curing (optimised at 150 °C) show high CC (1133.33 mmol/kg) with DS of 0.183 and yield of 87 % (dry weight. Interestingly, we observe that PC gels are thermally cross-linkable (***Figure 5.1*(d-h)**), which led to their improved structural

integrity under wet conditions (***Figure 5.2***), solving the general problem of hygroscopicity encountered with cellulosic materials. The mechanistic understanding of phosphate-based functionalization and its heat-induced cross-linking were investigated through ATR-FTIR, XPS and $^{13}C/^{31}P$ solid-state NMR spectroscopy. The present study reports an energy-efficient, low-cost, scalable strategy for the production of 3D printable PC gels with improved rheological behaviour, structural integrity, and hydro-stability for potential dye remediation.

5.2.2 LCA of PC gel and its comparative analysis

LCA for PC production was conducted to assess the ecological impacts and harmful emissions and compared with traditionally produced TEMPO-oxidized MFC. From ***Figure 5.3*****(a-c)** it can be observed that TEMPO-oxidized MFC generated higher impacts in comparison to DAHP-based phosphorylation in case of all environmental impact parameters. In climate change category (biogenic carbon), TEMPO-oxidation route generates highest impact of ~11-11.5 kg CO_2 eq., which reduced to almost half ~6.86 kg CO_2 eq. in case of PC gels. For fossil depletion, TEMPO-oxidation generates 2.62 kg oil eq. whereas PC generates a comparatively lowered impact of 1.5 kg oil eq.

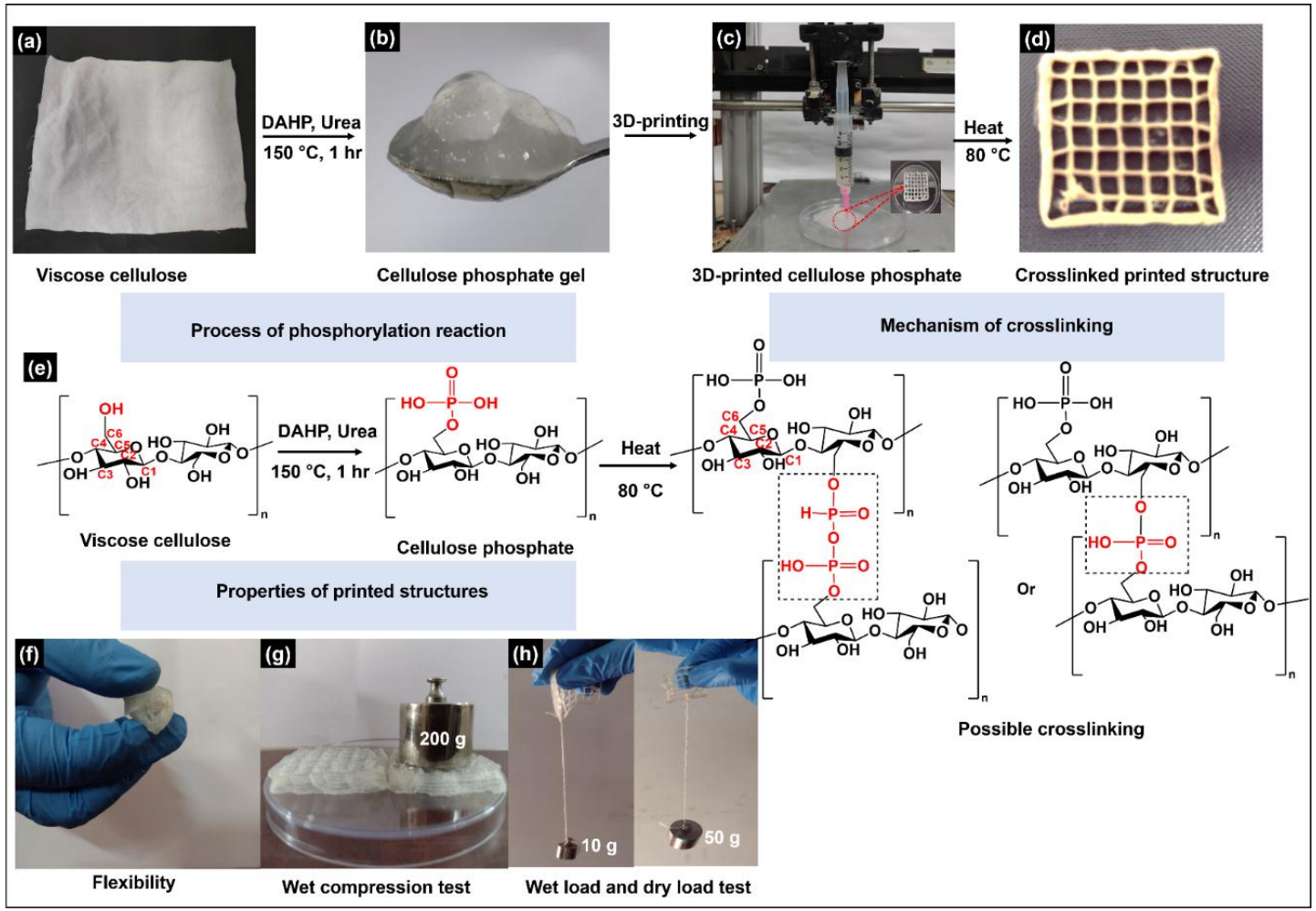

Figure 5.1 *(a-d) Schematic route for production of 3D-printed PC, (e) mechanism of phosphorylation and heat-induced crosslinking, (f) flexible structure, (g-h) mechanically stable 3D-printed structures with compression load of 200 g and tensile load of 50 and 10 g.*

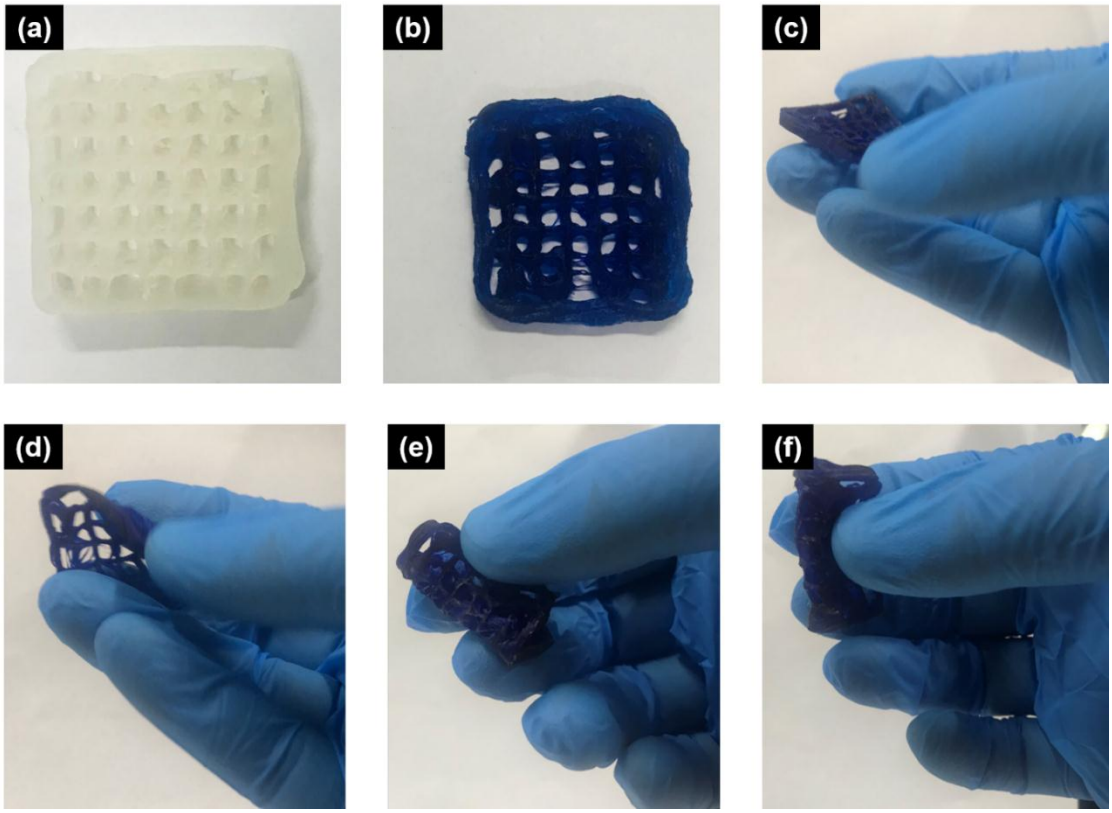

Figure 5.2 *(a) 3D-printed structure, (b) structure after MB adsorption, and (c-f) flexibility of the dye-adsorbed PC structure.*

Similarly, terrestrial ecotoxicity impacts of TEMPO- oxidation was 0.991 kg 1,4-DB eq., which was reduced to 0.444 kg 1,4-DB eq. in PC. For human toxicity (non-cancer), TEMPO-oxidation generates 0.144 kg 1,4-DB eq. while in the case of phosphorylation, it reduces by half to 0.072 1,4-DB eq. From the LCA result, it was observed that TEMPO-oxidation as a chemical modification strategy generates higher ecological impacts and greenhouse gas emissions arising from increased electricity and chemical consumption. In contrast, phosphorylating agents are agro-based chemicals such as urea and DAHP with lower energy requirements, making them an environmentally friendly and sustainable alternative.

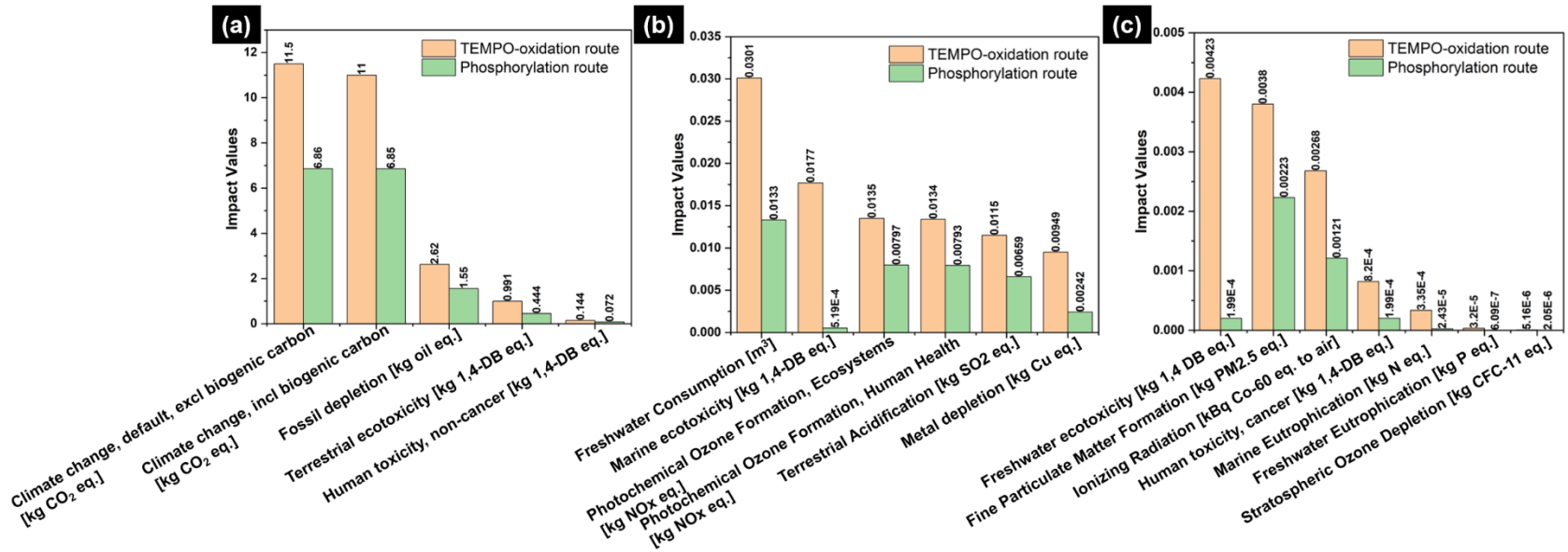

Figure 5.3 *Impacts generated in different categories for PC production and TEMPO-oxidation (a) impact generated in climate change (excluding and including biogenic carbon), fossil depletion, terrestrial toxicity, and human toxicity (non-cancer, (b) freshwater consumption, marine ecotoxicity, photochemical ozone formation (human health and ecosystem), terrestrial acidification, and metal depletion, and (c) freshwater ecotoxicity, fine particulate matter formation, ionizing radiation, human toxicity (cancer), marine eutrophication, freshwater eutrophication, and stratospheric ozone depletion.*

5.2.3 Rheological behavior of PC gel

The linear viscoelastic (LVR) region of all samples are studied from amplitude sweep plot, shows storage modulus (G') and loss modulus (G'') are independent of applied shear strain. From ***Figure 5.4*****(a)**, LVR region shows similar characteristics in region of 0.01 % applied shear rate for all samples. In PC gel with solid content of 5.5 % (PC@5.5 %), LVR region experienced disruption after shear strain of 0.01 %. G' rises with increased shear rate, while G″ decreased with increasing shear rate before reaching crossover points at shear strain of 0.053 %. Similarly, PC@4.9 % and PC@4.3 % displayed a comparable trend to PC@5.5 %, with crossover points occurring at shear strains of 0.046 % and 0.026 %, respectively. The findings suggest that before cross-over point, all samples exhibited solid-like characteristics, but afterward, elastic component became more prominent with transition to fluid-like behaviour.

Steady-state viscosity as a function of shear rate with a rise in solid content of PC shows an increase in viscosity (***Figure 5.4*****(b)**). On increasing shear rate, a drastic decrease in viscosity shows shear-thinning behaviour of PC gels was observed at all concentrations. This is due to the disruption of hydrogen bonds and entangled cellulose fibrils on applied shear. Furthermore, shear thinning behaviour of PC gels were studied using power law model for calculation of k (consistency index) and n (power law index) parameters (***Figure 5.4*****(f)**) [476]. The k rises as solid content of PC increases and n decreases for PC@5.5 % (0.319), and PC@4.9 % (0.168) with maximum n ~0.344 for PC@4.3 %. For all PC samples n <1, which makes it suitable for printing but low k for PC@4.9 % gels lead to minimum consistency [477].

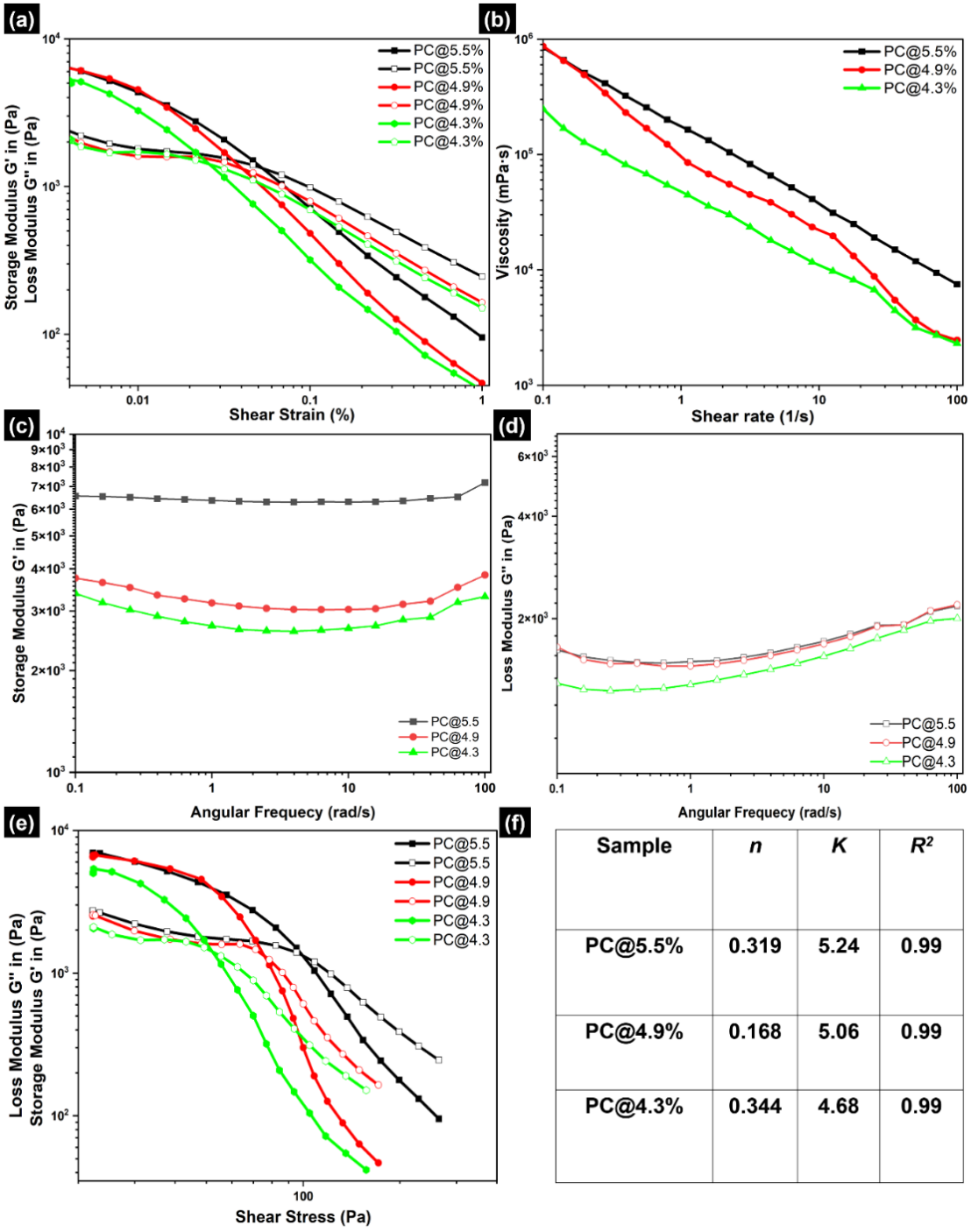

Sample	*n*	*K*	R^2
PC@5.5%	0.319	5.24	0.99
PC@4.9%	0.168	5.06	0.99
PC@4.3%	0.344	4.68	0.99

Figure 5.4 *Rheological properties (a) storage modulus (G′) and loss modulus (G″) as a function of shear strain (LVR region), (b) viscosity vs shear rate to calculate the power law parameters, (c-d) G′ and G″ as a function of angular frequency at various solid content, (e) G′ and G″ vs shear stress and (f) measured shear thinning parameters of gels. Solid and open symbols represent G' and G'', respectively.*

In ***Figure 5.4*(c-d),** with increasing PC solid content, *G′* and G″ remain independent of applied frequency, with solid-like behaviour. Similarly, G″ vs frequency plots for PC@5.5% and PC@4.9% showed similar characteristics with maximum G″ of 1647 and 1617 Pa and minimum for PC@4.3% (1289 Pa) (***Figure 5.4*(d)**). From ***Figure 5.4*(e)**, G' and G" decrease in all three solid contents with a crossover point at 100.49 Pa, 74.78 Pa, and 52.18 Pa for PC@5.5%, PC@4.9%, and PC@4.3% respectively. After the cross-over point, G" becomes greater than G' , indicating that PC gels lose their solid-like behaviour to fluid-like characteristics due to the weakening of entanglements [478]. The investigation of the rheological properties of PC gels suggests its easy and effective 3D printability through additive manufacturing techniques for producing scalable and value-added products.

5.2.4 Evaluation of functional properties of PC

The conductometric titration curve (***Figure 5.5*(a)**) shows a large plateau region with three inflexion points, revealing that two -OH groups in PC have been titrated. This is probably due to the presence of two acidic moieties and one phosphate group in the cellulose backbone forming Cell-O-P(O)$(OH)_2$ ***Figure 5.1***. The acidic moieties present undergo protonation/de-protonation at different pHs, which were evaluated through zeta-potential studies. The PC gels show uniform negative charge with zeta potential varying from -15.5 mV to - 47.5 mV over pH range ~2 to 11 **((*Figure 5.5*b)).**

FTIR analysis was carried out to confirm the phosphorylation (***Figure 5.5*(c-d)**) and evaluate appropriate functional groups in PC gels with their corresponding wavenumber mentioned in ***Table 5.1***. FTIR spectrum of VC, shows characteristics peaks for cellulose at 896 cm^{-1}, 1052 cm^{-1}, 1106 cm^{-1}, and 1428 cm^{-1} correspond to C_1-H deformation, C-O-C pyranose ring skeletal vibration, C-O stretching , and C-H

bending respectively [225,277,479–481]. The IR peaks at 1626 cm^{-1} are related to the vibration of absorbed water molecules, 2887 cm^{-1} represents the C-H functional group in stretching vibrational mode, 3334 cm^{-1} and 3342 cm^{-1} correspond to stretching vibration O-H molecules [480,482,483] which were present in both PC and VC. The Peaks at 1156 cm^{-1}, 1311 cm^{-1}, and 1370 cm^{-1} are related to C-O-C asymmetric stretching of cellulose, $-CH_2$ in-plane bending, and C-H bending [480,482] were also present in both VC and PC. The peaks at 1023 cm^{-1} and 1455 cm^{-1} in PC are assigned to the vibration of C_1-H deformation groups [484,485]. In FTIR spectra of PC, new peaks were observed at 783 cm^{-1}, 830 cm^{-1}, 922 cm^{-1},1023 cm^{-1}, 1252 cm^{-1}, 1455 cm^{-1}, and 2360 $cm^{-1,}$ which correspond to C–H out-of-plane ring deformation [486], P-O-C aliphatic bond [225], P-O-P antisymmetric vibration [487], P=O vibration due presence of orthophosphate diester bond [225], and P-H stretching vibration [205] respectively. The presence of phosphate vibrations suggests possible phosphorylation of VC; however, to further confirm covalent bonding of phosphate to cellulose backbone, XPS and solid-state NMR spectroscopy were carried out.

***Figure 5.6*(a)** shows the XPS survey of VC and PC and the % atomic of elements *C*, *O* and swith an area of *O1s*, P2p, and *C1s* curves tabulated in

Table 5.2*.** In VC, peaks at 286.08 eV and 532.07 eV represent the *O1s* and *C1s* bonds, respectively. The high-resolution peak of *C1s* of VC (Figure 5.6*(c)**) convolutes into three peaks, 286.4 eV, 284.7 eV, and 287 eV representing C-O, C-C and C=O bonds, respectively. The full width at half maximum (FWHM) of all peaks are 1.34, 1.19 and 2.09 respectively. The C=O bonds in the VC are associated with the bonding of carbonyl and acetal groups in cellulose, especially the *C3* position [488].The presence of sharp and distinct peaks at 134.08 eV, 285.08 eV, and 532.08 eV in PC (

Figure 5.6*(b))** convolutes into three peaks at 284.8 eV, 286.1 eV, and 288.8 eV corresponding to C-C, C-OH, and O-C-O bonds respectively with the associated FWHM values of 1.11, 1.62 and 2.01 respectively[17,489]. In high-resolution *O1s* (**(*Figure 5.6*(d))** spectra of PC, shows sharp and distinct peak at 531.4 eV and 533.1 eV confirms presence of P=O and P-O-P respectively, with peak at 532.4 eV in VC represents C-OH bond. The conversion of C-OH bond into P=O or P-O-P bond confirms the successful phosphorylation of VC [490]. The FWHM values of *C1s*, *O1s* and *P2p* are below 2.5 eV, which is acceptable for fitting the XPS data [491]. *P2p* spectra of PC (**(*Figure 5.6*(b)**) at 133.7 eV (1.26 FWHM) and 133.2 eV (1.99 FWHM) are assigned to C-P-O and P-O respectively, which is strong evidence for effective incorporation of phosphate groups [492–494]. This confirms phosphorylation with formation of covalent linkages on cellulose backbone, mechanism of which was further confirmed through solid-state NMR studies as discussed in subsequent section. ^{13}C and ^{31}P spectral analysis using solid-state NMR was performed to evaluate the presence of phosphate nuclei on PC and VC (Figure 5.6*(e-h)**). The *C6*, *C4*, and *C1* carbon positions in cellulose are represented by a range of NMR peaks at 58–68 ppm, 80–91 ppm, and 101–109 ppm [190,221,234,495], respectively. The peaks between 68–80 ppm of cellulose ring correspond to the *C2*, *C3*, and *C5* positions [255]. In ***Figure 5.6*(e),** the ^{13}C spectra of the VC show peaks at 63.8 ppm and 76.3 ppm, corresponding to *C6* and *C2*, *C3*, and *C5* positions of the cellulose ring, respectively. The peaks within the 83.7-90.2 ppm range signify the *C4* position, while those in the 106.2-108.5 ppm range indicate the *C1* position of the cellulose [255]. ***Figure 5.6*(f)** shows ^{13}C spectra of PC with a peak at 102.6 ppm, which represents *C1*, which is connected to two oxygen atoms. The peak at 80.8 ppm corresponds to *C4* in the amorphous region. The peak at

62.09 ppm represents an amorphous and crystalline region of *C6*, and the signal at 73.1 ppm corresponds to *C2*, *C3*, and *C5*. No detectable peaks were observed in the ^{31}P spectra of VC in ***Figure 5.6*(g)**, indicating the absence of phosphate groups before phosphorylation. The peaks in the range of -10 ppm to 10 ppm confirm the incorporation of phosphate groups at positions *C2*, *C3*, and *C6* due to the formation of phosphate ester bonds. The sharp peak at 0.53 ppm confirms successful phosphorylation, which leads to the covalent linkage of phosphoric monoester after the substitution of free hydroxyl groups in cellulose, as shown in ***Figure 5.6*(h)**. The sharp peak at 10.89 ppm implies partial condensation of phosphoric ester groups in PC during heat treatment, which enables cross-linking of cellulose chains similarly observed in polyphosphates and earlier reported studies [27]. The ^{13}C spectra of VC and PC shows similar characteristics peaks of cellulose backbone with slight shift in the peak position and decrease in intensity after phosphorylation across all the ranges [221]. Therefore, solid-state NMR studies confirm the presence of phosphate in cellulose backbone through covalent linkages and their cross-linking on heat treatment.

Table 5.1 *FTIR spectra peaks of VC and PC and their corresponding functional groups.*

FTIR peaks (cm^{-1})	Representative functional groups
830	P-OH
896	C_1-H deformation with vibration
1052	C-O-C pyranose ring skeletal vibration
1105	C-O stretching
1428	C-H bending vibration
1626	Deformation vibration of water molecules
2887	C-H functional group in stretching Vibrational mode
3334	Vibration O-H molecules
1156	C-O-C asymmetric stretching of cellulose

1311	-CH_2 in-plane bending
1370	C-H bending
1023	C_1-H deformation with vibration
1455	N-H functional groups
922	P-OH bond
1023	P-O-P antisymmetric vibration,
1252	P=O vibration
1455	Orthophosphate diester bond
2360	P-H bond
783	P-C vibrational absorption

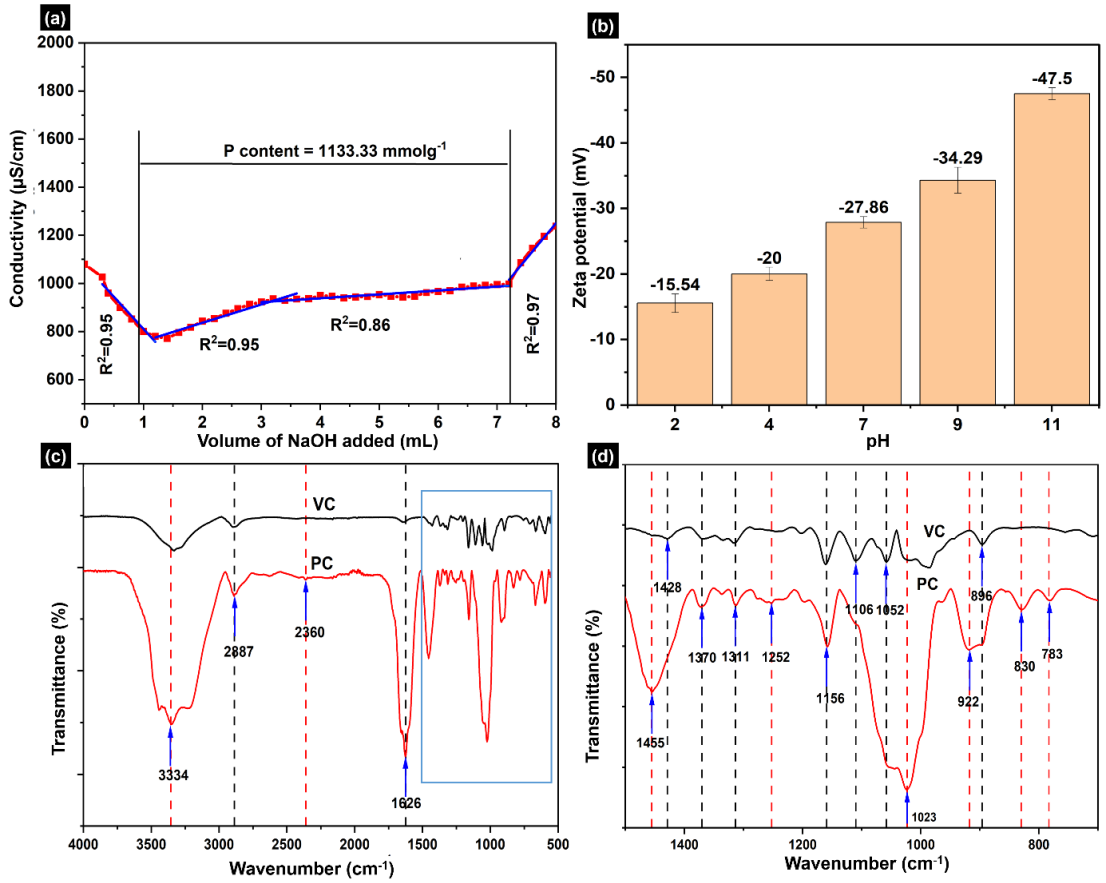

Figure 5.5 *Presents (a) conductometric titration, (b) zeta-potential at different pH levels, (c) FTIR spectrogram full range, and (d) spectra in the range 1400-800 cm^{-1}.*

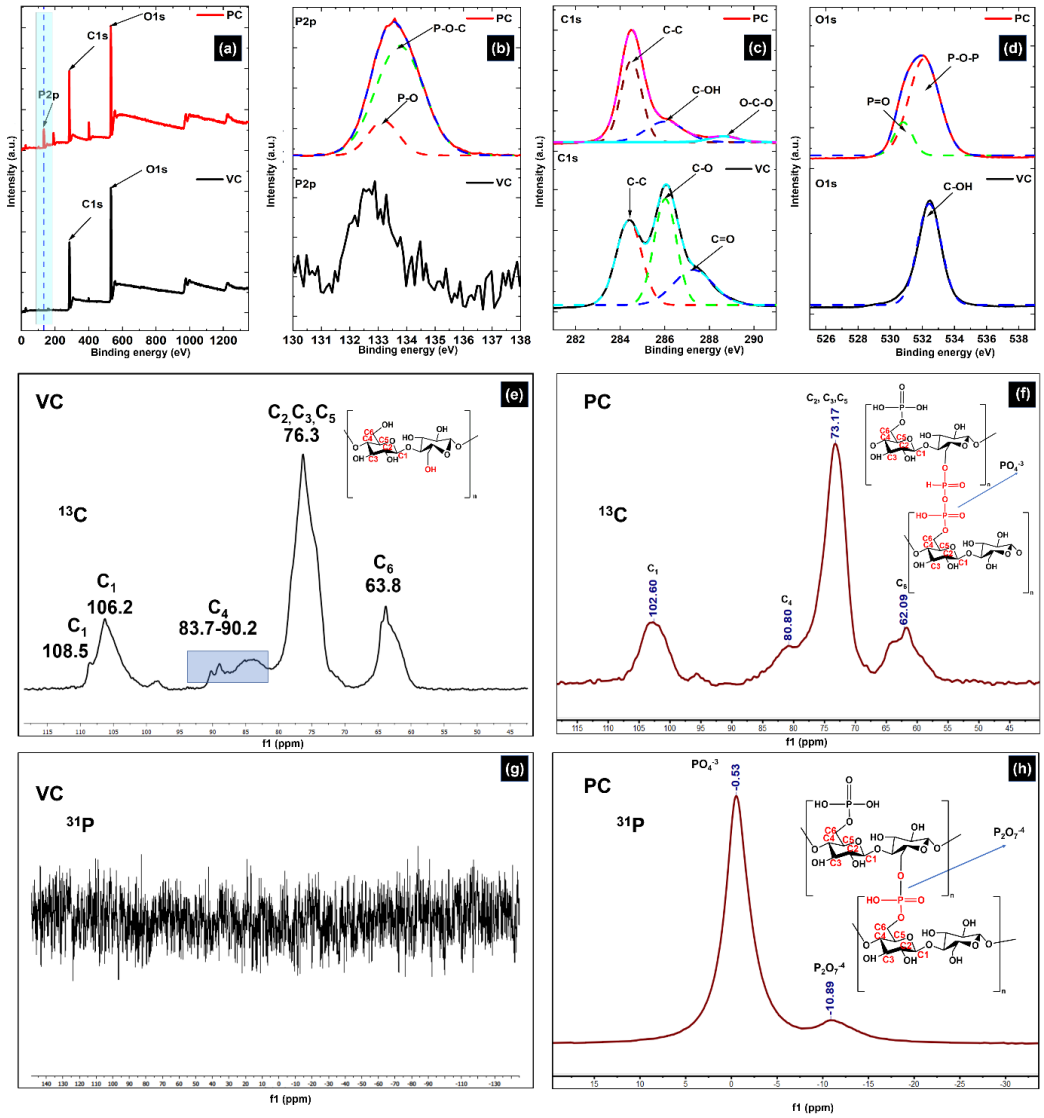

Figure 5.6 *Presents (a) XPS survey, high-resolution spectra of (b) P2p, (c) C1s, (d) O1s of VC, solid-state NMR (e-f) ^{13}C of VC and PC and (g-h) ^{31}P of VC and PC.*

Table 5.2 *Physiochemical properties of 3D printed PC structures.*

Parameter			
pH	**3**	**7**	**11**
Swelling (%)	406	532	700
Water uptake (%)	3400	3900	5408.3
Atomic (%) XPS	*O1s*	*C1s*	*P1s*
VC	36.44	63.41	0.15
PC	38.35	52.24	9.42
TGA	$T_{onset\ (10\ \%)}$	$T_{(50\ \%)}$	**Residual mass**
VC	303.01	343.52	3.86
PC	181.27	328.27	36.10

5.2.5 Water uptake and swelling behavior of 3D printed PC

Swelling behaviour of PC structures under various pH conditions were carried out to assess their structural stability in acidic or alkaline environment due to change in surface charge of PC as also confirmed from zeta potential studies. Additionally, the study evaluated appropriateness of 3D-printed structures for the adsorption of MB at different pH levels. The swelling behaviour of hydrogels is influenced by several factors, including the appropriateness of solvent, pH, degree of crosslinking, and ionisation of functional groups. After immersing the PC structure in water for 24 hours at pH of 3, 6.8, and 11, water uptake capacity was found to be 3400 %, 3900 %, and 5408.3 %, respectively (***Table 5.2***). Furthermore, the swelling capacity of the PC structure under the same conditions was 406 %, 532 %, and 700 %, respectively. As pH increases, the ionisation of phosphate groups (which are anionic) also increases, resulting in more hydrophilicity and greater swelling capacity [496]. Due to hydrophilic nature and the negative phosphate charge on its surface, PC exhibits repulsive interactions among intra and inter-molecular cellulosic chains. This phenomenon causes the network to swell, enhancing its ability to absorb water molecules. Under acidic conditions at pH ~2-3, the high concentration of H_3O^+ ions led to the protonation of phosphate anions (PO_4^{-3}) in PC, which led to a significant decrease in the swelling ratio as the pH decreased. Under alkaline conditions (pH 10-11), the increased abundance of OH^- ions in the solution and negative charge on the PC surface induced stronger electrostatic repulsion. This ultimately caused more significant swelling of the microfibers within the PC structures. Similar types of swelling behaviour of cellulose were also reported by other studies by Kaseem et al. [497], Arafa et al. [498], and Cagnin et al. [499].

5.2.6 Evaluation of structural and thermal properties of VC and PC

XRD analysis was performed to investigate the effect of phosphorylation on the crystal structure of cellulose (***Figure 5.7***) XRD spectra of VC show three distinct peaks at 2θ of 15.6°, 22.5°, and 34.6° corresponding to planes ($1\bar{1}0$), (200), and (004) [500]. PC shows three distinct peaks at 16.8°, 22.5°, and 36.6° assigned to (110), (200), and (004), respectively, crystal planes of cellulose [277,501–503]. Phosphorylation led to a peak shift in PC from 15.6° to 16.8° and 34.6° to 36.6° due to curing treatment at higher temperatures. The values of *d*-spacing, crystallite size, and FWHM of VC and PC at different crystal planes are detailed in ***Table 5.3***. It was observed that *d*-spacing of PC at ($1\bar{1}0$) reduced to 5.05 *Å* from 5.60 *Å* in VC, however, it remains unchanged for plane at (200). The diffractogram of VC and PC showed no significant changes, indicating that the polymorphic form of cellulose remained unchanged after the phosphorylation. The *C.I.* of VC was measured to be ~77.13 %, which was reduced to 65.48 % in PC after the phosphorylation reaction. The thermal degradation of cellulose occurs due to dehydration, depolymerization, and char formation of glycosyl residues [496]. The thermogravimetric curve for VC and PC shows one-step degradation (***Figure 5.7*****(b))** with parameters mentioned in ***Table 5.2***. For VC and PC, the first stage of weight loss of ~ 4 % was observed from 30-120 °C. This weight loss is mainly due to the evaporation of water or moisture present in both VC and PC [242,496]. T_{onset} (10 % weight loss) of both VC and PC occurred at 303.0 °C and 181.2 °C, respectively. Moreover, T_{50} (50 % weight loss) of VC was observed at 343.5 °C, which reduced to 328.2 °C for PC. This is possibly due to the formation of low molecular weight cellulosic chains during curing at high temperatures and high CC, which catalyses the depolymerisation of cellulose backbone [242,275,482]. The percentage mass residual

at 700 °C in the case of VC was 3.86 %, which increased to 36.1 % in PC, possibly due to the high CC of phosphate groups and increased char formation. Even though PC has low thermal stability, increased char formation at high temperatures >350 °C leads to their possible application as flame retardant materials.

Table 5.3 *Represents the FWHM value, d-spacing, and crystallite size of VC and PC.*

2-Theta (θ)	**FWHM**	***d*-spacing *(A^o)***	**Crystallite size *(A^o)***
15.6	3.13	5.6	0.467
16.8	2.34	5.05	0.626
22.5	4.91	3.94	0.30

5.2.7 Mechanical properties of 3D printed PC structures

The structural stability of the 3D printed PC was evaluated under both tensile and compression load for several cycles before and after dye remediation. The 3D printed structures before dye adsorption show maximum tensile strength and modulus of 3.25 MPa and 21.10 MPa, respectively (***Figure 5.7*****(c))**. After dye adsorption, the 3D printed structures show a brittle nature with a lowered tensile strength of 0.567 MPa and modulus of ~22.68 MPa. Cyclic compression for multiple cycles was carried out to study the compressive strength and modulus of 3D printed structures under wet conditions. The cyclic compression plot shows a nonlinear curve with an almost identical hysteresis loop in all five cycles, indicating PC gel's elastic characteristics (***Figure 5.7*****(d))**. Even after five stress cycles, an identical hysteresis loop suggests high reversibility and preservation of PC gel's elastic properties even after 50 % compression of its initial height. The results indicate a mechanically robust and structurally stable PC with elastic characteristics under both tensile and compression load, making it suitable for engineering applications.

5.2.8 Morphological studies of 3D printed PC

SEM analysis was carried out to understand the morphological properties of 3D-printed PC structures, as shown in ***Figure 5.8*(a-d)**. The micrograph in ***Figure 5.8*(a)** represents the 3D-printed structure of a PC having an average grid size of 0.47 mm. The high-resolution micrograph shows a network of aligned microfibers in the grid, which is possibly due to the direction of printing **(*Figure 5.8*(b))**. ***Figure 5.8*(c) and *Figure 5.8*(d)** show densely aligned thick aggregated cellulose microfibers, which could be due to the crosslinking of PC during drying at 80 °C. The elemental mapping confirms the uniform distribution of phosphate groups (***Figure 5.8*(e-h)**) with a content of 10.32 atomic % and 4.62 weight %.

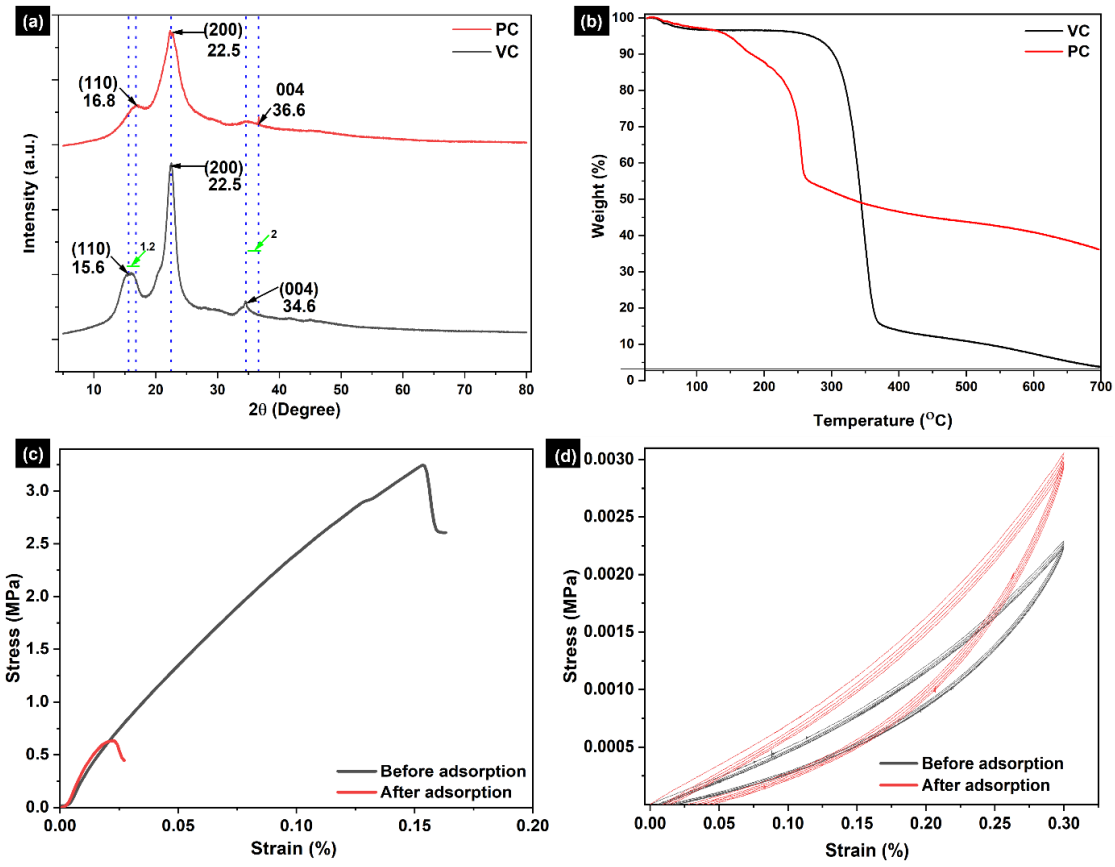

***Figure 5.7** Presents (a) XRD diffractogram, (b) TGA thermogram of VC and PC, (c) tensile property, and (d) compressive property of 3D- printed PC structures.*

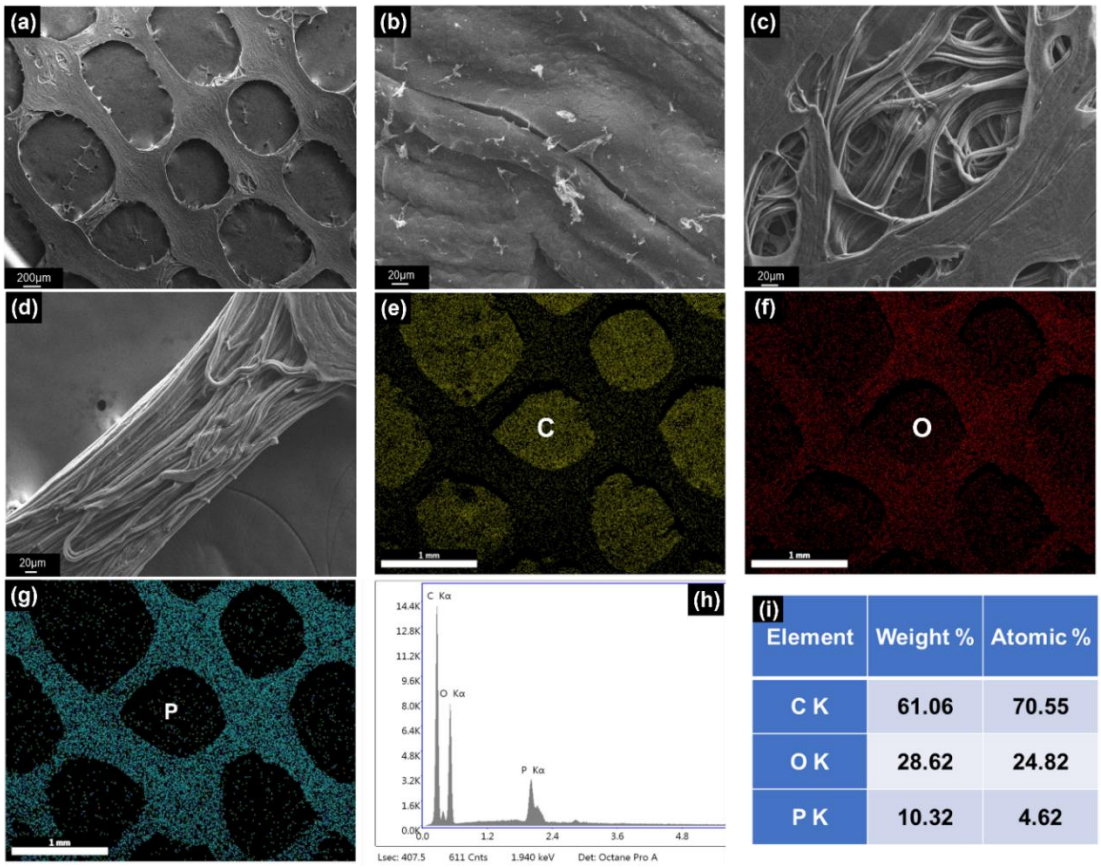

Element	Weight %	Atomic %
C K	61.06	70.55
O K	28.62	24.82
P K	10.32	4.62

Figure 5.8 *SEM micrographs of (a)3D-printed PC structure, (b), and (c) at high magnification, (d) showing aligned cellulose fibres with elemental mapping for distribution of (e) Carbon(C), (f) Oxygen(O), (g) Phosphorous(P) and (h-i) EDS spectra with respective atomic and weight %.*

5.2.9 Dye Adsorption and its kinetics studies

5.2.9.1 Effect of initial concentration and contact time on adsorption behaviour

The adsorption behaviour of 3D-printed PC structures was examined by varying MB dye concentration and contact time. From ***Figure 5.9*****(a)**, excellent MB adsorption performance (> 99 %) was observed for concentration range ~10 to 200 mg/L, which reduced to 94.8 % and 83.6 % at high MB dye of 300 and 500 mg/L, respectively. Further, the effect on adsorption was studied at different contact times (0-1440 minutes) over the MB range of (10-500 mg/L) (***Figure 5.9*****(b))**. With the increase in contact time, adsorption capacity increases until the plateau region is observed at which saturation is

reached. At the initial stage, the easy availability of active sites on the surface of 3D printed PC adsorbent results in a higher rate of adsorption followed by a stagnant region, suggesting adsorption has attained equilibrium with the saturation of all active sites [457,504]. At lower concentrations (10-60 mg/L), equilibrium was achieved within 240 mins, which increased to 1080 min at high concentrations (500 mg/L). Recent studies on the adsorption of MB and other heavy metals using PC have been mentioned in ***Table 5.6.*** The presence of high charge density of phosphate groups in PC greatly influences the adsorption efficiency and percentage removal of MB.

5.2.9.2 Effects of temperature on MB adsorption

The adsorption phenomenon between the adsorbate and adsorbent are regulated by temperature as shown in ***Figure 5.9*****(f).** The % removal of MB varied between 97 to 99.5 % for temperature range 20-50 °C indicating that adsorption phenomenon is driven by endothermic reaction. There was a minimal rise in % removal of MB on increasing the temperature. An increase in temperature can expedite the movement of dye molecules, fostering enhanced interaction between the adsorbate and adsorption sites present on surface of adsorbent [58]. Furthermore, elevated temperatures may induce a swelling effect in the internal structure of the PC structures, facilitating the permeation of dye molecules and consequently leading to an increase in MB adsorption. Similar trends of minimal improvement in adsorption at increasing temperatures was found by Ghouti et al. and Somsesta et al. using cellulosic olive stone biomass and activated carbon cellulose bio-composite film respectively [457,505].

5.2.9.3 Effects of pH on MB adsorption

MB typically occurs in two states: one with prevalent positive charges, prominent in acidic environments, and second with the zwitterionic species, which is present in alkaline conditions [506]. The change in pH affects the surface charge of dyes as well as adsorbate, therefore, influence of pH on dye adsorption was investigated and shown in the ***Figure 5.9*****(g).** The result indicates that the % removal of MB is highest in a basic medium (pH 11), equivalent to 99 %, while in an acidic (pH 2) solution, it is reduced to 84 %. This is due to existence of MB zwitterion in the alkaline pH [506] and the dominance of high negatively charged phosphate (PO_3^{-4}) content on the surface of 3D printed structures, improves the electrostatic interaction with cationic charges of MB [507]. A similar observation was reported by Boukind et al. Olivito et al., Said et al. and Somsesta et al. found that MB remediation using PC shows excellent adsorption in highly basic medium [277,505,508,509].

5.2.9.4 Adsorption kinetics

Two kinetic models were fitted with the experimental data and were found to have *R*-squared (R^2) values of 0.80-0.95 for pseudo-first-order (PFO) and 0.98-0.99 for pseudo-second-order (PSO) kinetics, as mentioned in ***Table 5.4***. The above results indicate that MB adsorption on the surface of a 3D printed structure follows PSO kinetics (***Figure 5.9*****(c)**), which signifies that chemisorption influences dye remediation. A similar observation by Suflet et al. and Boukind et al. using monobasic cellulose phosphate for dye remediation followed PSO kinetics [277,510].

Table 5.4 *Kinetic parameters for PFO and PSO*

Dye concentration (mg/L)	K_1 (PFO)	R^2	K^2 (PSO)	R^2
10	0.00428	0.85254	0.01557	0.98994
20	0.00266	0.91493	0.01438	0.99831
40	0.00287	0.88035	0.008115	0.99853
60	0.00343	0.94264	0.002903	0.9956
80	0.00397	0.96368	0.003413	0.99814
100	0.000864	0.80773	0.00158	0.994
120	0.00133	0.83242	0.000833	0.98262
150	0.00441	0.9556	0.001383	0.99683
200	0.00293	0.88742	0.000972	0.99711
300	0.00259	0.9326	0.000757	0.99704
500	0.00218	0.86938	0.000383	0.99227

Intra-particle diffusion model was fitted with experimental data to study mechanistic behaviour of MB adsorption on 3D-printed PC adsorbent. In ***Figure 5.9*****(i),** a plot between Q_t and $t^{1/2}$ shows three linear regions representing that diffusion of MB onto PC adsorbent occurred in three phases. In first phase, a sharp increase in external mass transfer of MB from solution to surface of adsorbent occurs which is evident from steep slope of the graph 0.43514 $mg^{-1}min^{-1/2}$. The second phase shows gradual increases in adsorption which is controlled by interfacial diffusion with diffusion rate constant (K_i) and boundary layer thickness (C_i) found to 0.166 $mg^{-1}min^{-1/2}$ and 2.51 mg/g respectively. The last phase corresponds to equilibrium stage where adsorption take place on internal surface of PC and show gentle rise in slope by 0.00447 $mg^{-1}min^{-1/2}$. The decrease in K_i suggests increased resistance in mass transfer with slower rate of intraparticle diffusion due to saturation of active sites and reduced MB dye remaining in aqueous phase.

5.2.9.5 Adsorption isotherms

To understand the interaction of PC structures with MB, three different isotherms (Langmuir, Freundlich, and Temkin) were evaluated. For Langmuir isotherm, the data was fitted against C_e / Q_e versus C_e with correlation coefficient (R^2) of 0.992 as shown in ***Figure 5.9*(d)**. Freundlich isotherm plotted against $log\ Q_e$ versus $log\ C_e$ shows lower R^2 ~0.472, whereas, Temkin isotherm plotted between Q_e and $ln\ C_e$, shows R^2~0869. It was observed that Langmuir isotherm well fitted suggesting that adsorption is monolayer mediated homogenously over the surface of adsorbent with parameters tabulated in ***Table 5.5***. Similar observations were found with PC samples (Alfa-P, MCC-P, and wood-P) in which Langmuir isotherm fitted best with experimental data for dye adsorption [244,511].

Table 5.5 *Isotherm parameters for Langmuir, Freundlich and Temkin isotherm.*

Isotherm	**k_L (*L/mg*)**	***Q_e(mg/g)***	***R^2***
Langmuir isotherm	0.64	30.55	0.99262
Freundlich	k_F ((mg/g) (L/mg)1/n	n	R^2
	2.58	0.322	0.47296
Temkin	A_T (L/mg)	b_T (J/mol).	R^2
	49	3.52035	0.86946

5.2.9.6 Adsorption thermodynamic

Thermodynamic parameters such as entropy, enthalpy, and Gibbs free energy greatly influence adsorption behaviour and can be determined from adsorption isotherm (***Table 5.7***). ΔS^o and ΔH^o were calculated from the intercept and slope of the plot between $ln\ K_c$ and $1/T$ in ***Figure 5.9*(g)**. ΔG^o were found to range from -1.6 to - 8.23 kJ/mol for a temperature range of 293-318 K indicating that the adsorption phenomenon onto 3D printed PC structure is spontaneous and thermodynamically more favourable.

Moreover, positive entropy shows an increased degree of randomness and level of disorder with a positive ΔHº value, which affirms that adsorption is endothermic [457].

5.2.9.7 Dye adsorption-desorption study

The reusability of an adsorbent helps in sustainable use, minimizing overall operation costs and reducing the disposal burden in any remediation process. The adsorption study of MB on 3D-printed PC structures for six different adsorptions and desorption cycles was studied, as shown in ***Figure 5.9*****(h)**. The high desorption rate of an adsorbent depends on the nature of its interaction with the adsorbate. In an acidic medium, protonation of the adsorbent surface starts due to reduced electrostatic interaction for positively charged adsorbate (MB). Due to decreased electrostatic interaction, MB diffuses from the active site of the adsorbent into the regeneration solution, resulting in desorption [512]. The adsorption efficiency of MB over the seven cycles did not change much, and it was found to be close to ~99 % throughout the experiments. However, the desorption efficiency reduced from 93 % to 70 %.

Table 5.6 *Thermodynamic parameters of adsorption process.*

Temperature (*K*)	***ΔG°* (kJ mol^{-1})**	***ΔH°* (kJ mol^{-1})**	***ΔS°* (J mol^{-1} K^{-1})**
293.15	-1.60	71.83	252.74
298.15	-3.85		
303.15	-5.44		
308.15	-6.13		
313.15	-7.20		
318.15	-8.23		

Table 5.7 *Comparitive table for the removal of MB and heavy metals using PC.*

Material (Phosphorylated)	Concentration range (mg/L)	Dyes/heavy metals	Removal percentage	Fitted kinetic and isotherm model	Reusability	Ref.
PC from Giant reed	0-2000	MB	92-99 %	PSO and Langmuir isotherm	2 cycles	[277]
MCC	0-2000	MB	99 %	PSO and Langmuir isotherm	-	[509]
Alfa grass, wood, and	0-1000	MB	55-100 %	-	Upto 6 cycles	[244]
Moringa olifera	10	Rhodamine B	83 %	-	-	[304]
CNF	10-500	Uranium	80-85 %	PSO and Langmuir isotherm	-	[298]
PC microsphere	30	Tetracycline	>90 %	PSOand Freundlich isotherm	-	[513]
PC nanostructured	2500	Chromium	88-93 %	-	-	[213]
Viscose	10-500	MB	99-83 %	PSO and Langmuir isotherm	7	**This work**

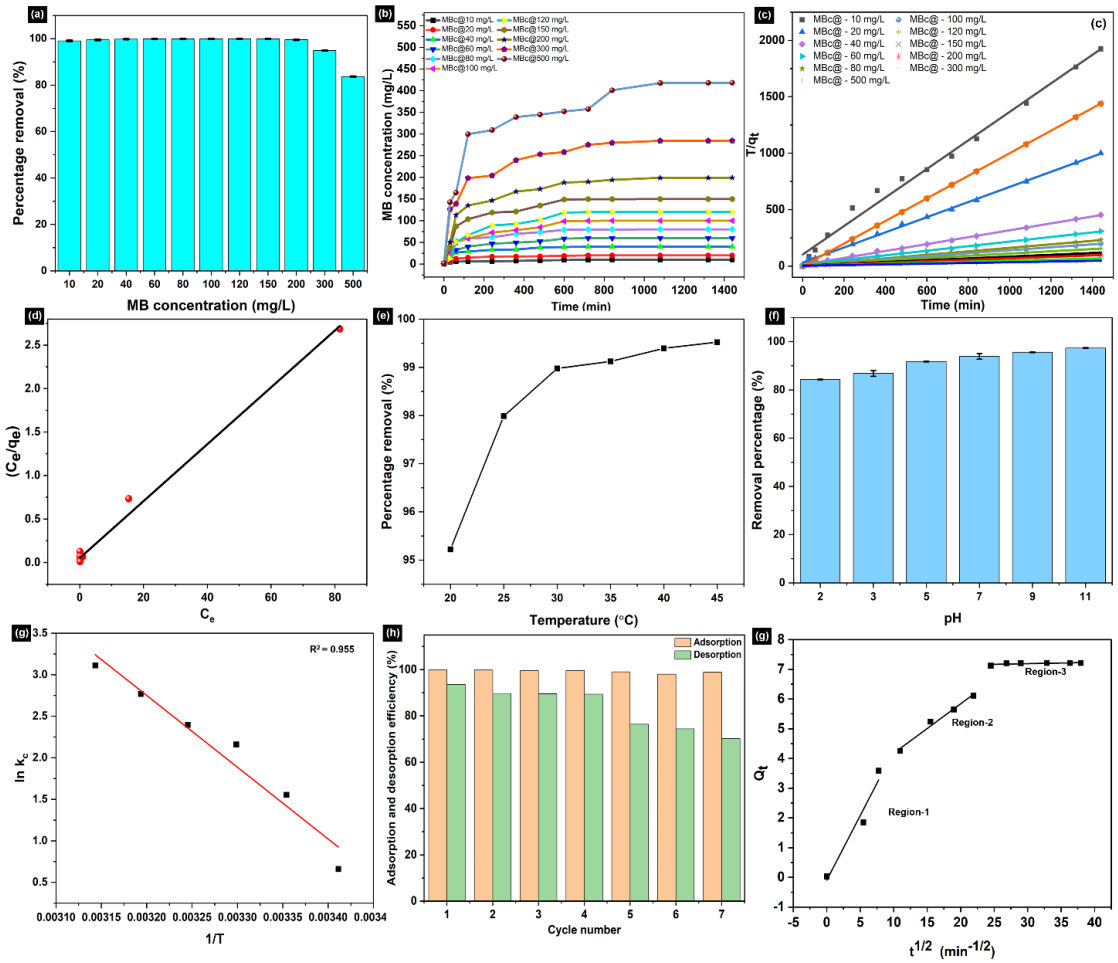

Figure 5.9 *Percent removal of dye at different (a) concentrations, (b) contact time, (c) fitted PSO kinetics, (d)Langmuir isotherm, (e) effect of temperature, (f) pH, (g) k_c vs temperature, (h) adsorption/desorption cycles and (i) fitted intraparticle diffusion model.*

5.3 *In-situ* modification of PC-3D printed structure

Figure 5.10 illustrates the scheme for fabrication of PC gel followed by its 3D printing for *in-situ* growth of MoS_2, and its subsequent utilisation for MB dye remediation. The present study involved treatment of VC with easily available low cost agro-based chemicals, DAHP and urea through a solid-state phosphorylation reaction to produce a 3D printable gel. The resulting PC exhibits viscous gel-like consistency with transparent texture and high-water absorption capacity. The production process of PC exhibits low environmental impacts with minimal reaction time and demands less energy as also evident from LCA studies. Subsequently, a combination of AMT salt/thiourea in different proportions was incorporated with PC to produce gels suitable for 3D printing, followed by *in-situ* growth of MoS_2. The rheological investigations indicated that the developed ink with the optimal proportion of AMT salt/thiourea shows viscoelastic properties with shear-thinning behaviour suitable for 3D printing. After hydrothermal treatment, transparent structures transformed to a black appearance, confirming *in-situ* growth of MoS_2, which were subsequently utilized for wastewater remediation consisting of photodegradation of MB and inactivation of microorganisms.

5.3.1 Rheological studies of gels

Firstly, the dynamic oscillatory sweep of the prepared gels was performed to investigate the linear viscoelastic region (LVR) region, as presented in ***Figure 5.11*****(a)**. The gels displayed LVR, predominantly within the shear rate of 0.01 to 0.1, where G' (storage modulus) and G'' (loss modulus) were unaffected by applied shear forces.

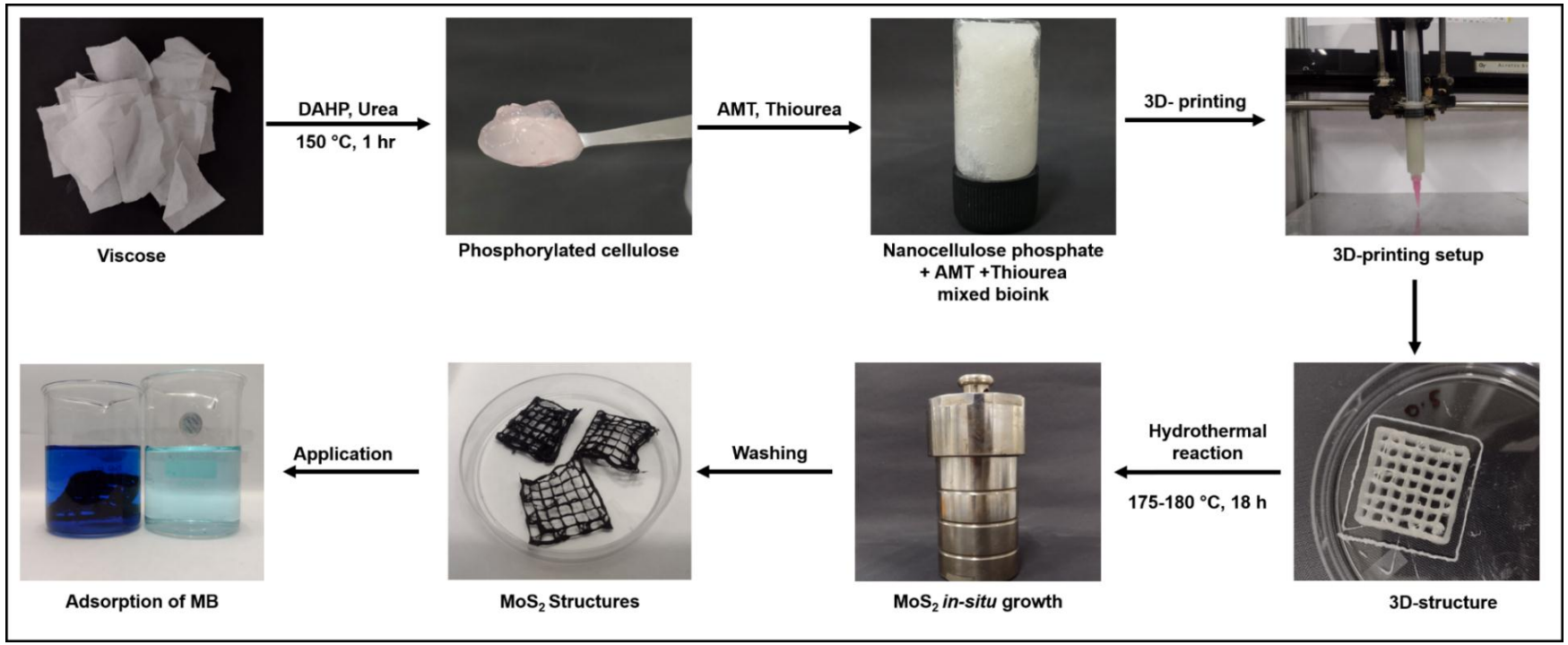

Figure 5.10 *Schema illustrates the production of PC and its subsequent 3D printing loaded with MoS_2 precursor salts. In-situ growth of MoS_2 on printed structures was performed via hydrothermal treatment which was then utilised for remediation of MB dye*

In this range, all developed gels demonstrated a rise in G' as the shear strain increased and at end of LVR (before the crossover point), all the gels showed solid-like behaviour. Beyond crossover point, the gels transitioned from solid-like characteristics to fluid-like behaviour, as indicated by higher G'' compared to G'. This change is due to decrease in viscosity of gels with increased shear strain, which leads to breakdown of internal structure due to weakening of bonding between cellulose fibrils.

5.3.1.1 Shear thinning properties of gels

The relationship between applied shear rate and viscosity were used to calculate gels consistency and flow index using the power law model, as shown in ***Figure 5.11*****(b)**. Flow index (n) describes the pseudo-plastic attribute of the gels, and consistency index (k) represents the consistency of gel formulation (values are mentioned in ***Figure 5.11*****(f))**. The viscosity of gels exhibited a decrease in response to increase in shear rate. The gel with highest salt concentration demonstrates maximum viscosity, due to potential interactions arising from negatively charged PC gel and positively charged molybdenum salts. The value of k for PCMo@0.5% (4.1), PCMo@0.75% (4.3) and PCMo@1% (4.5) were in range of 4.1-4.5, and for PC, PCMo@0.1%, and PCMo@0.25%, k were close to ~3.8. For all produced gels, n was found to be ~0.28-0.14 ($n<1$) indicating shear thinning behaviour, which makes them suitable for 3D printing applications [476].

5.3.1.2 Dynamic behavior of the gels

G' and G'' of produced gels as a function of angular frequency were shown in ***Figure 5.11*****(c)** and ***Figure 5.11*****(d),** respectively**.** ***Figure 5.11*****(c)** illustrates that G' for all the gels displayed similar trend which remains constant across entire range of

applied frequency. On increasing amount of salts in PC, G' was found to increase by ~1.5, 1.6, 2.1, 2.4, and 3.7 times for PCMo@0.1%, PCMo@0.25%, PCMo@0.5%, PCMo@0.75%, and PCMo@1% respectively in comparison to PC. ***Figure 5.11*****(d)** shows impact of gel concentration and angular frequency on their loss modulus (G''). Across entire range of applied angular frequency, all gels with added salts exhibits similar behaviour with no significant variation in loss modulus. However, PC showed frequency-dependent behaviour, possibly due to absence of charge-based interactions and formation of inter-molecular hydrogen bonding. The incorporation of salts in PC resulted in significant increase in G'' by ~0.9, 1.7, 1.8, 2.3, and 3.6 times for PCMo@0.1%, PCMo@0.25%, PCMo@0.5%, PCMo@0.75%, and PCMo@1%, respectively. PC gels with increasing salt concentrations shows higher $G' > G''$ in entire frequency range, indicating solid-like behaviour, arising from counter-ion charge based interactions[514,515]. ***Figure 5.11*****(e)** shows the relationship of G' and G'' against applied shear stress which depicts the structural and mechanical strength of prepared gels. The lowest value of G' was observed in PC (89.8 Pa), and the highest was in PCMo@1% (181.90 Pa). As the salt concentration was raised, there was a corresponding rise in the G' value. Based on ***Figure 5.11*****(e)**, it is also evident that as salt concentration increased, the yield stress of the gels also increased proportionally. These indicates that gels with higher salt concentrations would require higher forces during printing due to increased resistance in flow [476,516].

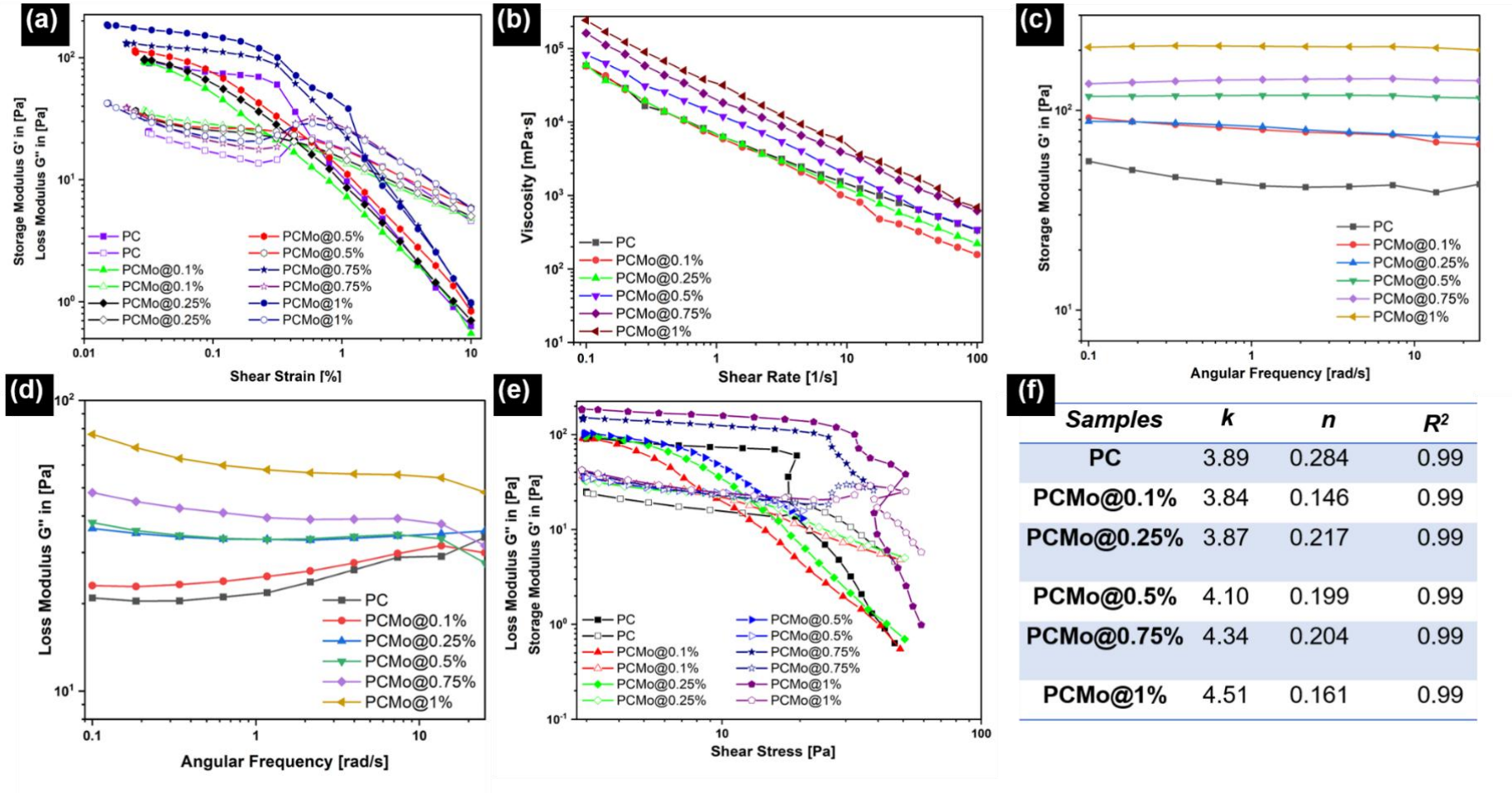

(f)

Samples	*k*	*n*	R^2
PC	3.89	0.284	0.99
PCMo@0.1%	3.84	0.146	0.99
PCMo@0.25%	3.87	0.217	0.99
PCMo@0.5%	4.10	0.199	0.99
PCMo@0.75%	4.34	0.204	0.99
PCMo@1%	4.51	0.161	0.99

Figure 5.11 *Rheological characteristics of gels (a) G' and G" versus shear strain, (b) viscosity against shear rate, (c) G' and (d) G" versus angular frequency (ω), (e) G' and G" against shear stress, and (f) power law parameters.*

5.3.2 Evaluation of functional properties

5.3.2.1 FTIR analysis of PC and *in-situ* grown PCMo structures

FTIR analysis was performed to understand the effect of phosphorylation reaction on VC and *in-situ* growth of MoS_2 on 3D printed PC structures after hydrothermal reaction, as presented in ***Figure 5.12*****(a-c)** and **(*Table 5.8*)**. The IR peaks at 615 cm^{-1}, 896 cm^{-1}, 1015 cm^{-1}, 1051 cm^{-1}, and 1162 cm^{-1} in PC gels correspond to P-O-C stretching vibration, asymmetric stretching of P-O-P linkage, P-O, P-O-C vibration, and C-O stretching of the pyranose ring, respectively [517–520]. The broad peak at 3340 cm^{-1} corresponds to O-H stretching, 1650 cm^{-1} represents carbonyl vibration and 1374 cm^{-1} represents C-H bending was found in all samples which confirms presence of PC backbone [298,374,477,521]. The peak at 1252 cm^{-1} corresponds to P=O vibration, mainly due to presence of an orthophosphate ester bond which confirms successful phosphorylation in PC [225]. PC gels with incorporated salts after hydrothermal treatment, shows IR peaks at 555 cm^{-1} and 605 cm^{-1} corresponding to Mo-S bond and peaks at 667 cm^{-1} represents Mo-O bond [522,523], which confirms successful growth of MoS_2 in 3D printed PC structures. The presence of distinct IR peaks at 555 cm^{-1}, 605 cm^{-1}, and 667 cm^{-1} in the samples indicates successful growth of MoS_2 on printed structures after hydrothermal reaction. In subsequent section, XPS and EDS studies were carried out to mechanistically understand and quantify the growth of MoS_2 on 3D printed structure.

Table 5.8 *FTIR spectra peaks with corresponding wavenumber and represented functional groups.*

FTIR peaks *(cm^{-1})*	Functional groups
555	Mo-S bonding
605	Mo-S bonding
667	Mo-O bonding
615	P-O-C stretching vibration
896	P-O-P linkage,
1015	P-O bonding and P-O-C vibration
1162	C-O stretching of the pyranose ring
1252	P=O ester bond
3340	O-H stretching vibration
1650	Carbonyl stretching vibrating
1374	C-H bending

5.3.2.2 XPS analysis PCMo@0.5%

Figure 5.12**(d)** presents full range XPS survey of PCMo@0.5% with peaks at binding energies ~283.0 eV, 133.0 eV, 230.0 eV, 162.0 eV, and 530.0 eV represent *C1s*, *P2p*, *Mo3d*, *S2p*, and *O1s* bonds respectively. In high-resolution spectrum of *C1s* (***Figure 5.12*****(e)),** peaks at 282.7 eV, 284.3 eV, and 285.5 eV represent C-Mo, C-C, and C-O-Mo bonds, respectively [524]. ***Figure 5.12*****(f)** illustrates the deconvoluted *Mo3d* spectrum of PCMo@0.5%, and peaks at 230.5 eV, 232.4 eV and 226.7 eV were assigned to $Mo3d_{5/2,}$ $Mo3d_{3/2}$ (indicating the +5-oxidation state of *Mo*) and *S2s* bond [525–527] respectively. ***Figure 5.12*****(g)** presents the broad XPS spectrum of *S2p*, and corresponding high-resolution peaks at 161.2 eV and 166.8 eV corresponds to $S2p_{1/2}$ and $S2p_{3/2}$, respectively [528,529]. In ***Figure 5.12*****(h),** the peak at 530.4 eV in broad spectrum of *O1s* represents to Mo-O or C-OH bonds [524,529,530]. In ***Figure 5.12*****(i),** high-resolution peak at binding energy of 133.3 eV corresponds to *P2p* (C−O−P

bond), and 131.70 eV was assigned to P-O bond [190,477,513]. The atomic percentages of *C*, *O*, *P*, *S*, and *Mo* mentioned in ***Table* 5.9** are in-line with EDX studies, discussed in subsequent section. The presence of *Mo*, *S*, and *P* peaks in XPS and FTIR spectra confirms the phosphorylation and *in-situ* growth of MoS_2 in 3D-printed PCMo@0.5%.

Table 5.9 *XPS analysis showing atomic percent of C, O, P, Mo, and S.*

C1s	***O1s***	***P2p***	***Mo3d***	***S2p***
57.87	29.24	0.85	0.45	1.93

5.3.3 XRD and Raman spectroscopy analysis of PC and *in-situ* grown PCMo structures

XRD was performed to understand the effect of phosphorylation and *in-situ* growth of MoS_2 on structural characteristics of PC. As shown in ***Figure 5.13*****(a)**, MoS_2 shows diffraction peaks at 2θ = 9.8°, 13.9°, 25.4° 29.2° 33.5°, and 59.3° corresponding to (002), (110), (101), (004), (103), and (110) lattice planes of *1T/1T'*-MoS_2 [446,531–534]. For PC, two characteristic peaks were observed at 2θ = 16.7° and 22.6°, corresponding to (110) and (200) crystal planes of cellulose I. The diffractogram of PC gels with *in-situ* grown MoS_2, shows three distinct peaks at 2θ = 12.4°, 20.0°, and 22.0° corresponding to lattice planes $(1\bar{1}0)$, (110), and (200) respectively, which represent characteristic peaks of cellulose II [87,535]. The conversion of cellulose I to cellulose II during hydrothermal treatment is possibly due to presence of thiourea or AMT with exposure to high temperature for prolonged time period. The presence of distinct MoS_2 peaks at 2θ = 32.8°, 35.4°, and 57.5° for all samples corresponds to crystal planes (100), (102), and (110), respectively shows formation of *2H*-phase of MoS_2 [536–538].

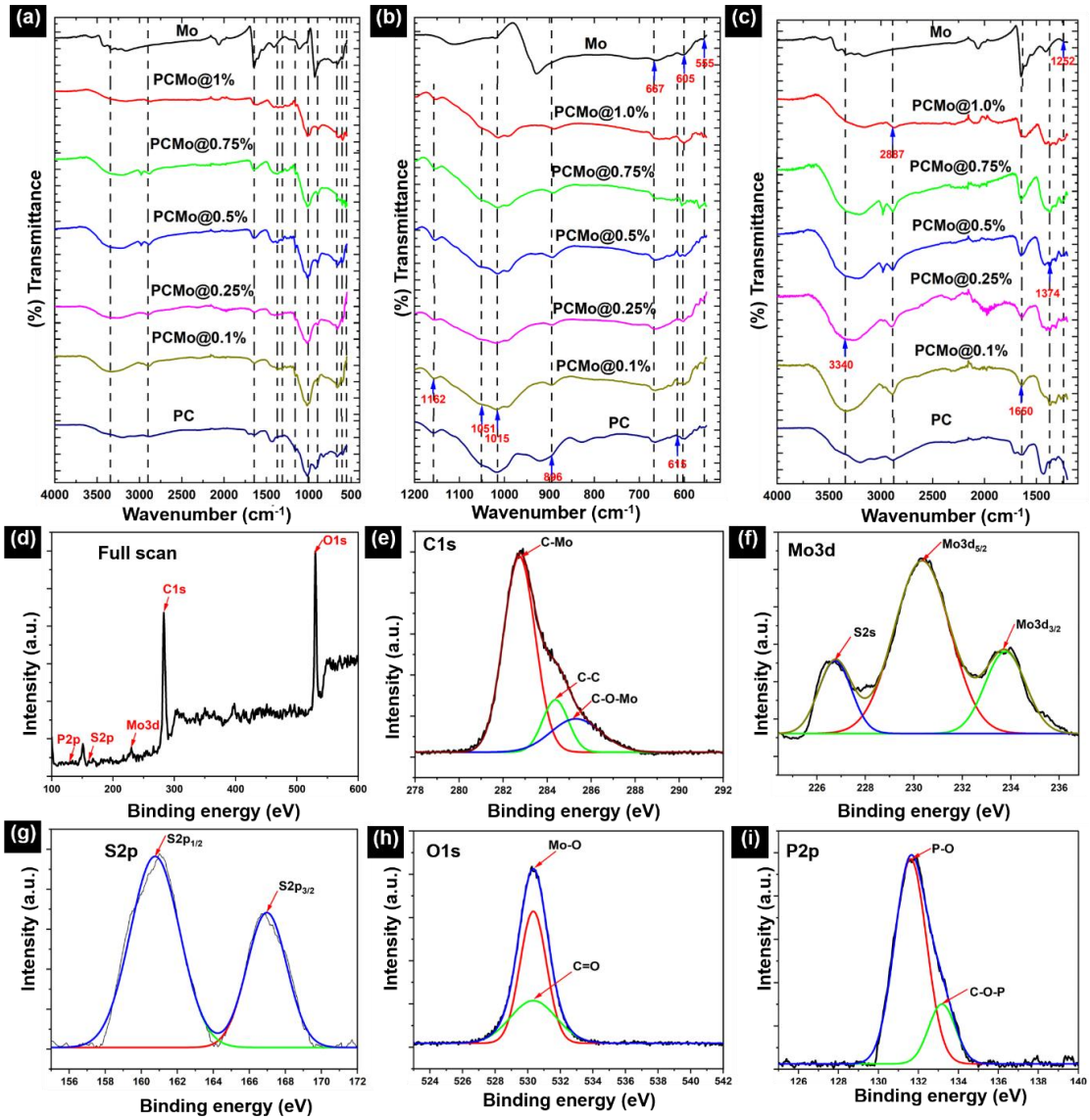

Figure 5.12 *FTIR spectrum (a) full range ~500-4000 cm^{-1}, (b) from 500-1200 cm^{-1}, (c) from 1200-4000 cm^{-1} and their corresponding peaks highlighted by blue arrows, (d) XPS survey of PCMo@0.5%, (e) high-resolution spectra of (e) C1s, (f) Mo, (g) S2p, (h) O1s and (i) P2p.*

XRD peaks at 2θ = 9.1° in PCMo@0.25% and PCMo@0.5% represent the crystal plane (002) of the *1T*-phase of MoS_2 [470,539]. The peak of MoS_2 at 2θ = 13.9° shifted to ~15.6° in PCMo@0.75% and PCMo@1% and to ~12.4° in PCMo@0.1% and PCMo@0.25%. Further, PCMo@0.25%, PCMo@0.5%, PCMo@0.75%, and PCMo@1% shows shift in peaks from 29.2° to 32.8°, 33.5° to 35.4° and 59.3° to 57.5° as compared to MoS_2. The shifting of peaks and inter-layer spacing were calculated

using Bragg's law as mentioned in ***Table 5.10.*** The shift in peaks is possibly due to increased MoS2 interaction with PC and precursor used for growth of MoS2 which led to increased interspacing between layers with intercalation of oxygen and ammonia originating from precursor salts [540,541].

Raman spectroscopy of developed composites (PCMo@0.5%, PCMo@0.75%, PCMo@1%) and Mo were performed to analyse the phase of grown MoS_2 (***Figure 5.13* (b)).** Raman spectrum shows peaks at 141.0 cm^{-1}, 233.0 cm^{-1}, 280.0 cm^{-1} and 333.0 cm^{-1} representing *J1*, *J2*, E_{1g}, and *J3* modes, respectively, confirming MoS_2 grown forms mixed *1T* and *2H*-phase [542,543]. The appearance of peaks *J1*, *J2*, and *J3* are ascribed to the superlattice configuration of *1T*-MoS_2, and the existence of the E_{1g} band at 378 cm^{-1} confirms the octahedral coordination of Mo in *1T*-MoS_2 [542,544]. Moreover, the Raman signals of A_g detected at 820 cm^{-1} and B_{1g} at 992 cm^{-1} can be attributed to symmetric and asymmetric stretching of terminal oxygen atoms. The presence of MoO_3 traces in MoS_2 is confirmed by the exclusive appearance of these peaks in spectra [542,545]. The peak at 378 cm^{-1} represents E^1_{2g} mode (57), and 661 cm^{-1} represents the A_g mode of the MoS_2 and the asymmetric stretching of the Mo–O–Mo bridge [546]. Therefore, XRD and Raman spectroscopy studies confirms presence of both *1T* and *2H*-phase which acts as cocatalyst and photosensitizer resulting in formation of stable photocatalyst, required for enhanced dye remediation and microbial inactivation.

Table 5.10 *XRD analysis showing peaks of MoS_2 and shifted peaks after modification.*

Mo peak, *2θ (°)*	***d*-spacing *(Å)***	**Shifted peak in composites *(°)***	***d*-spacing *(Å)***
9.8	9.01	9.13	9.68
13.9	6.27	15.6	5.68
33.5	2.67	32.8	5
59.3	1.556	57.52	1.60

5.3.4 Thermogravimetric analysis of PC and *in-situ* grown PCMo structures

Figure 5.13**(c)** displays thermogravimetric curves of PC and *in-situ* grown 3D printed MoS_2 structures, and their corresponding thermogravimetric parameters are presented in ***Figure 5.13*****(d)**. In case of PC and Mo, the initial decrease in weight of ~0.7 % and 2.2 % was noted during temperature range of 25 °C to 100 °C due to removal of trapped moisture within. For developed composites, first stage of weight loss of ~1.8 %, 3.0 %, 3.0 %, 1.9 %, and 3.9 % was observed in PCMo@0.1%, PCMo@0.25%, PCMo@0.5%, PCMo@0.75%, and PCMo@1% respectively in temperature range 25 °C to 100 °C. The onset thermal degradation temperature (T_{onset}), i.e., 10 % weight loss for PC, was observed at 184 °C due to decreased molecular weight and high phosphorylated CC of PC. For Mo, T_{onset} was found to be ~276 °C due to enhanced thermal stability of MoS_2 [470]. T_{onset} of PCMo@0.1%, PCMo@0.25%, PCMo@0.5%, PCMo@0.75% and PCMo@1% were found to increase to ~276 °C, 260 °C, 243 °C, 240 °C and 240 °C respectively compared to PC. PC's T_{max} (50 % weight loss) was observed at 261.6 °C due to thermal decomposition of cellulose backbone chains of PC and glycosyl unit [470]. In Mo, T_{max} was not observed due to high thermal stability of MoS_2, with percentage residual weight of 66.7% at 700 °C. T_{max} for PCMo@0.1%, PCMo@0.25%, and PCMo@0.5% were found to increase to 401 °C, 472 °C and 548 °C respectively,

which is due to growth of MoS_2 through strong hydrogen bonded interaction with PC [470,547]. The residual weight percentage of PC at 700 °C was 33.5 %, which increased to ~45-65 % with increasing inorganic content of MoS_2 concentration in 3D printed structures. From thermogravimetric studies it could be concluded that developed PC based MoS_2 composites have significantly high thermal stability which makes it ideal for potential dye or pollutant remediation.

5.3.5 Morphological studies

Morphological analysis of *in situ* grown MoS_2 and 3D printed grid structure of PCMo@0.5% are shown in ***Figure 5.14*****(a).** It was observed that hydrothermal treatment of 3D printed PC based MoS_2 composites led to shrinkage in the mesh size mainly due to high temperature-induced *in-situ* growth of MoS_2. However, it led to uniformly grown spherical-shaped clusters of size distribution ~1µm as can be seen in micrograph, ***Figure 5.14*****(b)** and at higher magnification in ***Figure 5.14*****(c)**. The micrograph of PCMo@0.5% reveals a surface with rough but evenly and compactly distributed MoS_2 on the fibrillated surface of PC (***Figure 5.14*****(d)**). A rough surface of PCMo@0.5% also helps in adsorption phenomenon by providing larger surface area for dye remediation. Furthermore, elemental mapping of PCMo@0.5% shows uniform distribution of *Mo*, *S*, and *P* which is in-line with the XPS studies confirming successful of *in-situ* grown MoS_2 onto surface of 3D-printed PC (***Figure 5.14*****(e-h)).**

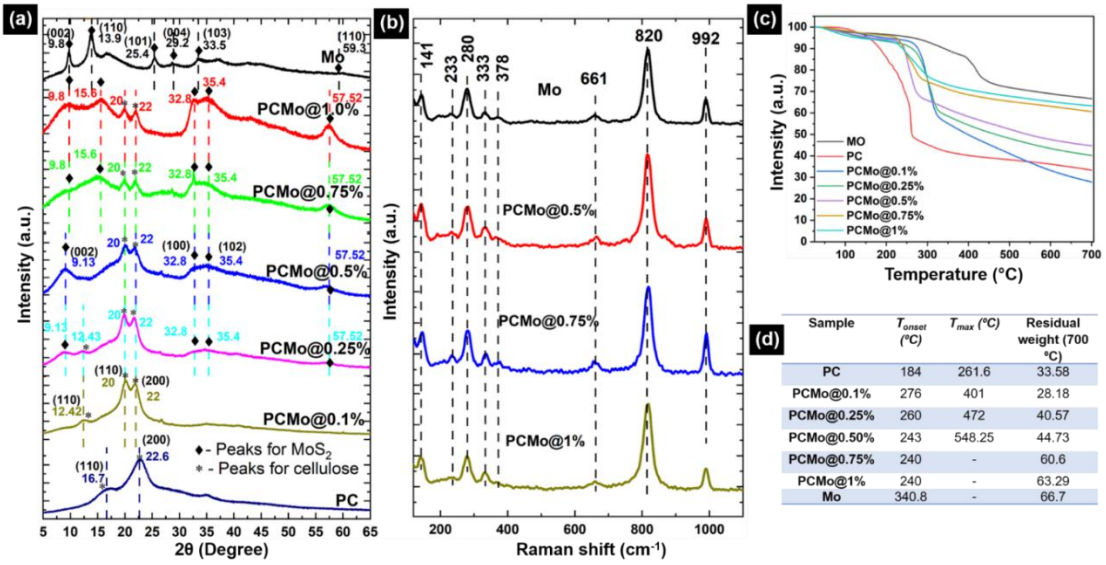

Sample	T_{onset} (°C)	T_{max} (°C)	Residual weight (700 °C)
PC	184	261.6	33.58
PCMo@0.1%	276	401	28.18
PCMo@0.25%	260	472	40.57
PCMo@0.50%	243	548.25	44.73
PCMo@0.75%	240	-	60.6
PCMo@1%	240	-	63.29
Mo	340.8	-	66.7

Figure 5.13 *(a) XRD, (b) Raman spectroscopy, (c) TGA and (d) measured thermal parameters for PC and PC based* MoS_2 *composites.*

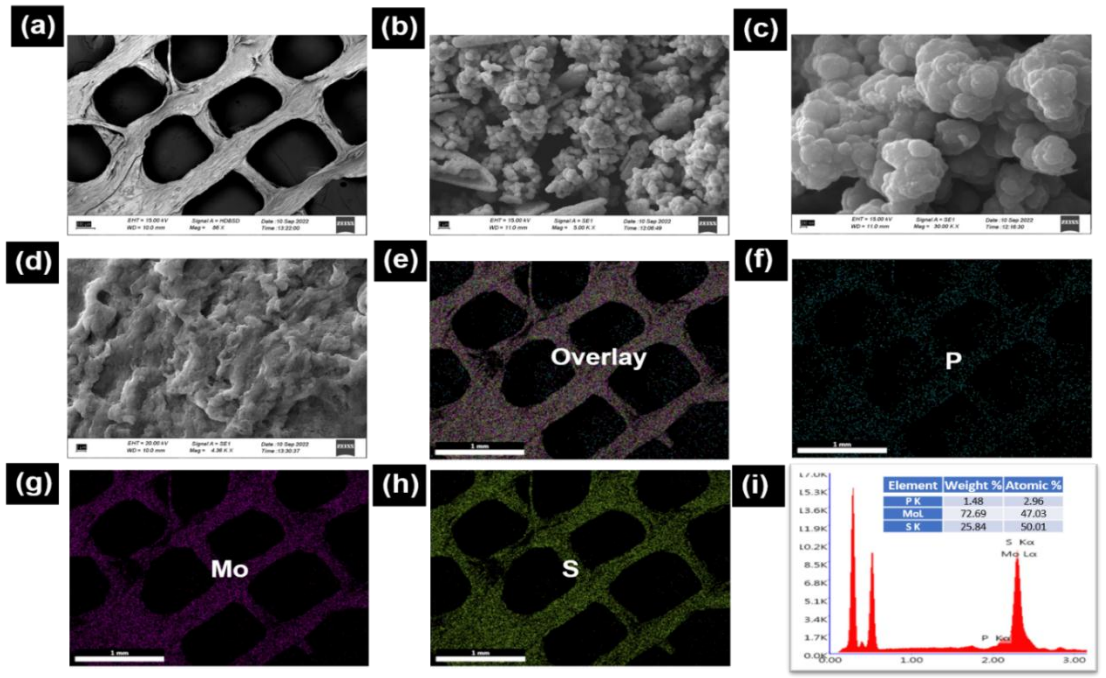

Figure 5.14 *SEM micrograph of (a) 3D printed structure including grids, (b) micrograph of Mo at lower and (c) higher magnification, (d) PCMo@0.5% with in-situ grown* MoS_2*, elemental mapping of PCMo@0.5%, (e) element overlay (f) P, (g) Mo, and (h) S, and (i)EDS spectra with its elemental weight and atomic percent (tabulated in inset).*

5.3.6 MB dye remediation using with *in-situ* grown 3D printed PC-based MoS_2

5.3.6.1 Effects of contact time and initial MB concentration on adsorption

The study investigated various MB concentrations (100-1000 mg/L) to assess the adsorption capacity of 3D printed PCMo@0.5% structures. It was found that the adsorption behaviour of MB consistently increased across the entire range of concentrations studied, as depicted in ***Figure 5.15*****(a)** and ***Figure 5.15*****(b).** In the first 30 minutes, there was sharp increase in adsorption percent of MB with an increase in contact time, due to presence of vacant active sites [373]. In the range of lower MB concentrations (100 - 500 mg/L), the adsorption process resulted in a removal percentage exceeding 99.0 %. However, for concentrations of 700 mg/L and 1000 mg/L, the percentage removal decreased to 95.5 % and 92.5 %, respectively. The PCMo@0.5% exhibited a maximum MB adsorption capacity of 464.1 mg/g. Consequently, as number of unoccupied active sites reduced, adsorption process entered state of stagnation with attainment of equilibrium, resulting in a minimal increase in adsorption percentage[150]. Similar observation were also reported by Qiu et al. for lead adsorption (52), Balakrishnan et al. [150] for MB adsorption and by Qin et al. [371] for Congo red adsorption on MoS_2 cellulose aerogel composites. This study's findings indicate PCMo@0.5% as highly efficient adsorbent material for removing dyes from wastewater.

5.3.6.2 Effects of temperature and pH on adsorption

The temperature is one of the critical parameters that help decide whether adsorption process is exothermic or endothermic. As illustrated in ***Figure 5.15*****(c),** an increase in temperature was observed to positively impact the adsorption process,

resulting in a notable enhancement in the percentage adsorption of MB. The maximum level of adsorption, corresponding to 99.8 %, was achieved when temperature reached to 45 °C. An increase in temperature enhances the mobility of dyes within an aqueous solution, leading to an increased interaction between the dye and adsorbate resulting in elevated rate of adsorption.

The pH of the solution significantly affects the adsorption process, as it impacts both the surface properties of the adsorbent materials and the ionisation of the adsorbate species. In ***Figure 5.15*****(d)**, it is demonstrated that as the pH of the MB dye solution increases, there is an observed increase in the extent of adsorption onto surface of PCMo@0.5%. The maximum percent of adsorption for MB was observed at pH~9, with percent adsorption of 99.3 %. Nevertheless, the adsorption percentages at pH 3, 7 and 6 were found to be 90.4 %, 99.3 %, and 99.1 %, respectively. Based on findings of the study, it can be concluded that enhanced adsorption of MB occurred on the negatively charged surface of PCMo@0.5% at higher pH levels, primarily through electrostatic interactions. This is consistent with the study, which observed that above pH 3, MoS_2 has a negative surface charge, which increases at higher pH and influences the adsorption process [548]. Gopalakrishnan et al. also similarly reported in their study that at alkaline pH, adsorption of MB increased on the surface of cellulose-MoS_2 and graphene hybrid adsorbent [150].

5.3.6.3 Adsorption isotherm

Two well-known isotherms models, namely Langmuir and Freundlich, were studied to investigate adsorption capacity of MB and its interaction with PCMo@0.5% **(*Figure 5.15*(e))**. These isotherms determine the extent of adsorption of MB on the distributed surface of PCMo@0.5% at equilibrium between the medium's liquid and

solid phases. The R^2 in the linearly fitted curve of Langmuir's and Freundlich's isotherms were found to be 0.98 and 0.88, respectively, and other isotherm parameters were tabulated in ***Table 5.11*.** These findings demonstrate that the Langmuir isotherm was well-fitted, suggesting monolayer adsorption mechanism favours the MB adsorption phenomenon on homogeneous surface of PCMo@0.5%.

5.3.6.4 Adsorption kinetics

The PFO and PSO kinetic models are widely studied for investigating mechanism and adsorption behaviour of MB dye on PCMo@0.5%. The experimental data were fitted in the PFO kinetic (graph plotted between log (Q_e - Q_t) versus time) and PSO kinetics models (t / Q_t versus time), as shown in ***Figure 5.15*(h)**. The R^2 values were observed in range of 0.78 - 0.98 for PFO and 0.99 for the PSO kinetics model (***Table 5.12*)**. This observation suggests that PSO kinetic governs the adsorption of MB on PCMo@0.5%.

According to principles of PSO kinetics, the adsorption process of MB onto PCMo@0.5% is predominantly governed by chemisorption, wherein there is an exchange or sharing of electrons between MB and 3D printed structure of PCMo@0.5%, arising from the photodegradation step. Gopalakrishnan et al. also observed similar findings in their study, wherein they fabricated composites of cellulose-MoS_2 and graphene to facilitate the photodegradation of MB [150].

Table 5.11 *Langmuir isotherm and Freundlich isotherm parameters.*

Langmuir isotherm			**Freundlich isotherm**	
B	***R^2***	***K_F***	***1/n***	***R^2***
0.18	**0.98**	7.136	0.4072	**0.886**

Table 5.12 *Adsorption kinetics of PFO kinetic and PSO kinetic with fitted R^2 values.*

Concentration (mg/L)	PFO kinetic		PSO kinetic	
	K_1	R^2	K_2	R^2
100	0.01608	0.96	0.002789	0.99
200	0.00004	0.99	0.001725	0.99
300	0.01042	0.95	0.001051	0.99
500	0.00806	0.96	0.000240	0.99
700	0.01687	0.78	0.000075	0.98
1000	0.00541	0.84	0.000070	0.98

Further, intra-particle diffusion model was studied to investigate the mechanistic response of MB adsorption onto PCMo@0.5%. In ***Figure 5.15*****(g)**, two linear regions indicated that the adsorption occurred in two steps on PCMo@0.5%. The linear regression analysis starts from the point of origin, suggesting that intra-particle diffusion is sole factor governing the rate at which MB molecules are adsorbed. During short time frame, there was a gradual improvement in the adsorption behaviour of MB [549,550]. The first region's slope represents intraparticle diffusion rate, and the intercept of first region represents thickness of boundary layer. In the second portion, adsorption occurred for a more extended time period and is related to the final equilibrium stage, where adsorption might happen in the adsorbent's internal structure or decrease due to lowered MB concentration. The values of K_i and C_i were calculated from the slope and intercept of first region, and were found to be~5.6 mg $g^{-1}min^{-1/2}$ and 0.9 mg/g, respectively.

5.3.6.5 Adsorption thermodynamics

The thermodynamic parameters such as enthalpy (ΔH), entropy (ΔS), and Gibb's free energy (ΔG) are associated with the adsorption process. The relationship between natural logarithm of K_c and reciprocal of temperature ($1/T$) was used to

determine ΔH and ΔS using slope and intercept, as depicted in ***Figure 5.15*****(f),** and their corresponding parameters are detailed in ***Table 5.13***. It was observed that on increasing temperature, ΔG decreases and negative sign of ΔG represents spontaneous behaviour of adsorption, with positive ΔH and ΔS affirm that adsorption occurs at surface of PCMo@0.5% was random and endothermic in nature.

Table 5.13 *Adsorption thermodynamic parameters.*

Temperature ***(K)***	ΔG^o ***(kJ mol^{-1})***	ΔH^o ***(kJ mol^{-1})***	ΔS^o ***(kJ mol^{-1} K^{-1})***
298.15	-2.13	119.24	0.406
303.15	-3.32		
308.15	-6.77		
315.15	-7.08		
318.5	-10.4		

5.3.7 Photodegradation of MB with PCMo@0.5%

Photocatalytic activities of PCMo@0.5% were investigated to study the degradation of MB under a white light source. A maximum photodegradation of ~99.0 % was achieved within 40 minutes for MB dye concentration of~100 mg/L, 200 mg/L, and 300 mg/L **(*Figure 5.15*(i))**. For high dye concentration of ~500 mg/L, 1000 mg/L and 700 mg/L MB photodegradation were found to reduce to 98.3 %, and 95.12 % after 80 min and 93 % in 100 minutes respectively. The photodegradation of MB was faster compared to adsorption due to the generation of superoxide radicals in PCMo@0.5% on exposure to light. As observed in earlier XRD and Raman spectroscopy studies, PCMo@0.5% contains MoS_2 with both *1T/2H* phases. The metallic *1T* phase serves as a co-catalyst along with the semiconducting *2H* phase, facilitating the efficient transfer of radicals and reducing the possibility of their recombination. This offers a sufficient number of accessible oxidising groups to efficiently breakdown a larger quantity of MB

molecules in the solution through photodegradation [551]. A low band gap in MoS_2 resulted in the generation of electrons and holes under simulated light conditions. Subsequently, electrons in the conduction band of MoS_2 reacts with surface oxygen, forming superoxide free radicals [552]. The generated superoxide free radicals in reaction with H^+ produce H_2O_2, which splits to form hydroxyl free radicals that are reactive leading to photodegradation of MB.

5.3.7.1 Reusability of PCMo@0.5%

The reusability of PCMo@0.5% was assessed by subjecting it to five consecutive cycles of MB degradation under light conditions. After analysing MB degradation following each cycle, it was observed that there was approximately~5.3% variation in degradation percentage after five consecutive cycles (***Figure 5.16*****(a)**) which shows exceptional reusability of PCMo@0.5%. The photodegradation of MB was conducted in continuous mode (***Figure 5.16*****(d)**) to assess its suitability for large-scale applications. The results indicate that MB photodegraded into smaller molecules continuously using 900 ml dye and 1 g of catalyst over 9 hours. The maximum degradation percentage achieved was 86 %, with a maximum photodegradation capacity of 77 mg/g.

5.3.7.2 Antibacterial properties of PCMo@0.5%

Antibacterial properties of PCMo@0.5% were studied on Gram-positive and Gram-negative *S. aureus* and *E. coli* respectively, at different loading concentrations. As shown in ***Figure 5.16*****(b-c),** the control portion from both plates showed no zone of inhibition for both bacteria. For Gram-positive *S. aureus*, at lower concentration of 0.1 % of PCMo@0.5%, a zone of inhibition of ~7 mm was observed.

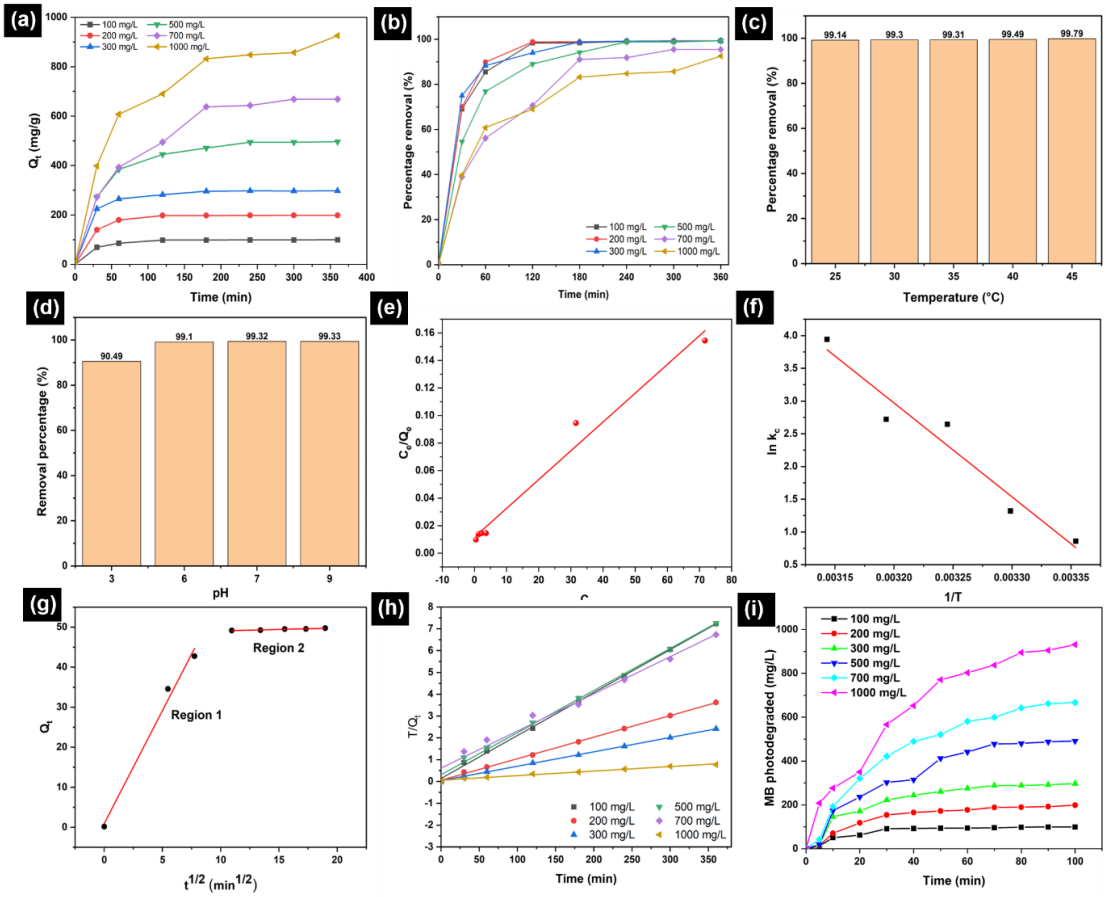

Figure 5.15 *Effect of dye adsorption (a) contact time, (b) percentage removal of MB, (c) temperature, (d) pH, (e) Langmuir isotherm, (f) thermodynamic of adsorption process, (g) intra-particle diffusion model, (h) PSO kinetics and (i) photodegradation of MB under light with intensity of 21.6 W/m^2.*

However, on increasing the concentration of PCMo@0.5% to 0.25 %, an increase in zone of inhibition to ~17 mm was found. On further increasing loading concentration to 0.5 %, no significant improvement in the zone of inhibition was observed ~14 mm. In case of Gram-negative *E. coli* with 0.1 % concentration of PCMo@0.5 %, a zone of inhibition of 5 mm was formed, which was comparatively lesser than *S. aureus.* When the concentration of PCMo@0.5% increased, to 0.25 %, a zone of 6 mm diameter was formed, which further increased to 8 mm diameter for 0.5 % concentration. This observation confirms the antibacterial properties in the developed PCMo@0.5%, which originates mainly due to the presence of MoS_2. On

exposure of light on MoS_2, it generates electrons and holes that react with water and oxygen molecules to generate reactive oxygen species which in turn inactivates or damages the cell walls of bacteria [553]. The reactive oxygen species generated gets embedded into the bacterial membrane creating dents on the membrane causing extraction of phospholipids and damages the integrity of the lipid cell membrane [554].

5.3.7.3 Continuous photodegradation and antibacterial properties of PCMo@0.5%

Real wastewater generally contains mixture of pollutants/dyes alongwith microbial contaminants therefore PCMo@0.5% was used to determine their dual function of dye remediation and decontamination through a continuous mode (as shown in ***Figure 5.16*****(d)**). A simulated solution containing MB dye as well as *E. coli* was continuously fed in a plug flow reactor containing the PCMo@0.5% catalyst. From ***Figure 5.16*****(f)** shows inhibition in growth of *E. coli* after three hours of continuous flow of media containing MB through a plug flow reactor. The degradation of dye as well as growth of bacteria was decreased, as shown in ***Figure 5.16*****(e)**, possibly due to the combined effect of photodegradation and antibacterial properties of PCMo@0.5%. As shown in ***Figure 5.16*****(f)**, the plating of MB dye solution containing *E. coli* shows growth of distinct colonies from t=1 to 5 hours. However, on passing the mixture through a plug flow reactor containing PCMo@0.5% in presence of light conditions, shows no growth in colonies of *E. coli* after t=2 hours. From the earlier reported studies it has been observed that MoS_2 can cause intracellular oxidative stress, membrane depolymerisation, disruption, and metabolic arrest [555] in the bacterial cell membrane or lipid membrane, leading to the bacteria's death [556]. Therefore, the present study provides a unique continuous mode and scalable approach for simultaneous

photodegradation of dyes/pollutants and microbial decontamination ideally suitable for treatment of high-volume real wastewater systems.

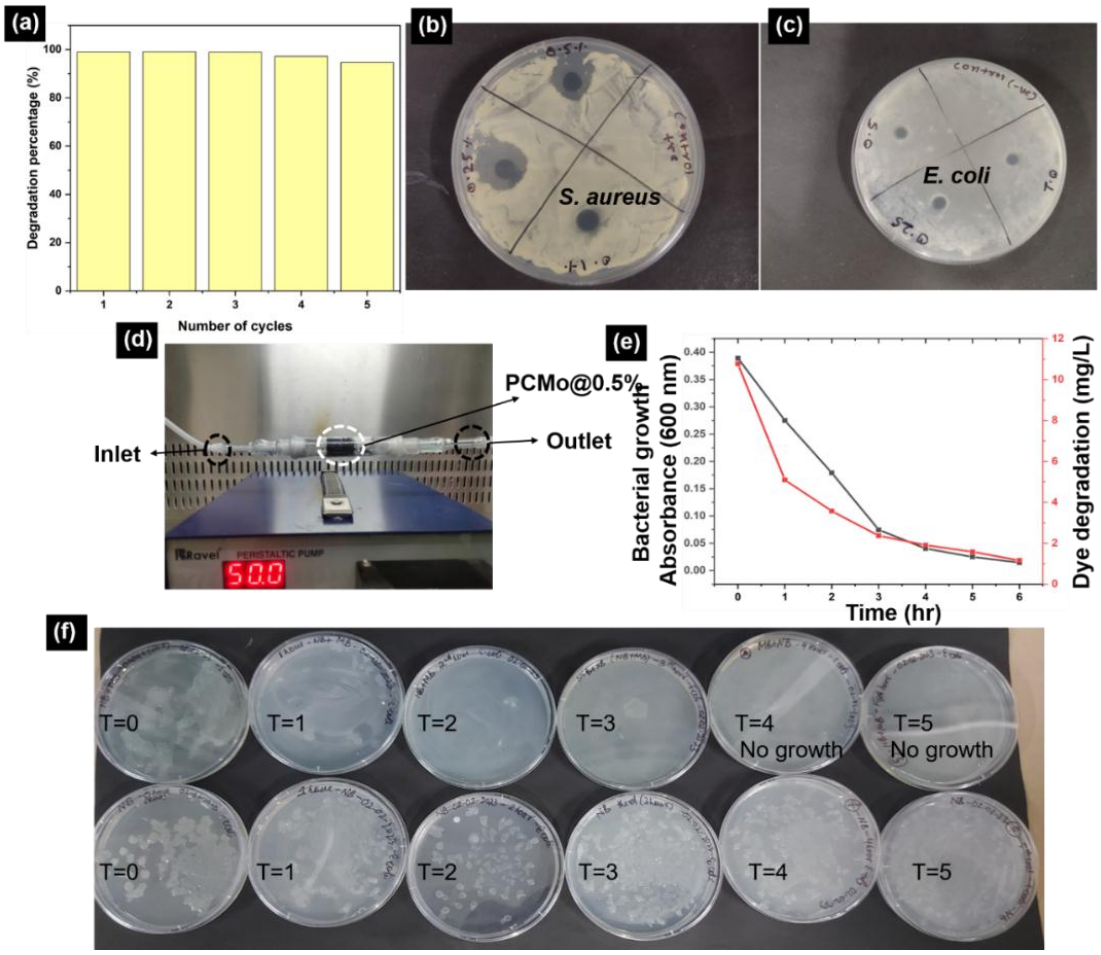

Figure 5.16 *(a)Reusability of PCMo@0.5%* for MB degradation, *antibacterial properties of PCMo@0.5% at different loading of 0.1%, 0.25% and 0.50% (b) S. aureus, (c) E. coli, (d) experimental setup for continuous degradation and decontamination, (e) and (f) effects of PCMo@0.5% on degradation of MB and antibacterial properties against E. coli.*

5.3.8 Mechanism of photodegradation

In photocatalytic oxidation process, when MoS_2 are exposed to visible light, the semiconductor is photoexcited, which results in formation of electron-hole pairs on the surface of the catalytic material, i.e., e_{CB}^{-} generates from conduction band. In contrast, h_{VB}^{+} is produced from the valence band. On the catalyst surface, oxygen vacancies serve as a trap for electrons to prevent electron-hole recombination.

$$MoS_2 + h\upsilon\,(vis) \rightarrow MoS_2\,(e_{CB}^- + h_{VB}^+) \quad \text{(eq.4)}$$

The electron generated from the applied photon oxidises with oxygen available on surface of MoS_2 generating superoxide free radical anions ($O_2^{\cdot -}$). The generated superoxide radical serves as a sink for the electron acceptor, which is represented as:

$$MoS_2(e_{CB}^-) + O_2 \rightarrow MoS_2 + O_2^{\cdot -} \quad \text{(eq.5)}$$

The organic molecule can quickly oxidise the photogenerated hole or react with either water molecules or a hydroxyl ion to generate a hydroxyl radical ($OH^{\cdot}$), as shown below:

$$MoS_2\,(h_{VB}^+) + H_2O \rightarrow MoS_2 + H^+ + OH^{\cdot} \quad \text{(eq.6)}$$

$$MoS_2\,(h_{VB}^+) + OH^- \rightarrow MoS_2 + OH^{\cdot} \quad \text{(eq.7)}$$

Finally, $O_2^{\cdot -}$ and $OH^{\cdot}$ free radical ions perform the overall photodegradation as shown in reaction below:

$$O_2^{\cdot -} + H_2O \rightarrow H^{\cdot}O_2 + OH^- \quad \text{(eq.8)}$$

$$H^{\cdot}O_2 + H_2O \rightarrow H_2O_2 + HO^{\cdot} \quad \text{(eq.9)}$$

$$HO^{\cdot} + C_{16}H_{18}ClN_3S\,(MB) \rightarrow CO_2 + H_2O \quad \text{(eq.10)}$$

Lastly, MB on reaction with highly reactive free hydroxyl radicals degraded into $CO_2 + H_2O$.

5.4 Summary

This chapter presents a comprehensive and innovative approach for the sustainable production of PC gels with enhanced properties through a green synthesis route. The utilization of agro-based chemicals in the phosphorylation process results in

transparent, negatively charged PC gels with high consistency, CC, and high degree of substitution (DS). The PC gels also showed excellent covalent crosslinking and thermal stability. The PC gels display shear-thinning properties enabling the smooth 3D printing of complex structures. The mechanism for covalent linkage and phosphate content were evaluated through detailed investigations of FTIR, EDS (~11.01%), XPS (9.42%), and solid state-NMR studies. The LCA studies reveal that CO_2 and other emissions is comparatively less than traditional TEMPO oxidation methods. Expanding upon this foundation, the research extends into the realm of additive manufacturing by incorporating MoS_2 *via* hydrothermal treatment, creating 3D printable PC structures with multifunctional capabilities. XRD and Raman spectroscopy studies shows the presence of MoS_2 with mixed *2H/1T* phase along with transition of cellulose I to cellulose II due to high temperature hydrothermal treatment in presence of urea derivatives. Furthermore, both the printed structures were utilized for the remediation of MB from wastewater. The PC structures also showed excellent stability in both acidic and basic environment, enabling the easy adsorption of MB without structural damage. The 3D printed PC structures show high adsorption capacity of 94.8-99% for MB dye concentration range of~300-500 mg/L. The synthesised PCMo@0.5% was found to display maximum adsorption and photodegradation of MB dyes, with adsorption capacity of ~464.16 mg/g in three hours. The photodegradation of MB also showed excellent results with maximum photodegradation of ~99.4, 99.1, and 99.1% for concentration range of 100-300 mg/L within 40 minutes. Reusability of PC structures shows that adsorption over seven-cycles led to 99% removal of MB dye, however, desorption range between 70-93% over seven cycles. The PCMo@0.5% was found to be efficiently recycled for photodegradation of MB upto 5 cycles with ~94.7%

efficiency. Interestingly, the synthesised PCMo@0.5% composites also showed combined antibacterial activity against *E. coli* and *S. aureus*.

Moreover, these 3D-printed structures exhibit continuous mode performance, making them promising candidates for the practical remediation of real wastewater at large volumes. The synergistic combination of sustainable PC production and the incorporation of MoS_2 through 3D printing presents a novel and environmentally friendly strategy for fabricating high-performance materials for wastewater remediation. This research opens up avenues for the development of value-added products with applications in various fields, emphasizing the importance of green, facile, and energy-efficient methodologies in advancing the frontier of PC and its composite.